Coupling of Stratospheric Warmings with Mesospheric Coolings in Observations and Simulations

CHRISTOPH ZÜLICKE, ERICH BECKER, VIVIEN MATTHIAS, AND DIETER H. W. PETERS

Leibniz Institute of Atmospheric Physics, Kühlungsborn, Germany

HAUKE SCHMIDT

Max Planck Institute of Meteorology, Hamburg, Germany

HAN-LI LIU

High Altitude Observatory, National Center of Atmospheric Research, Boulder, Colorado

LAURA DE LA TORRE RAMOS

Environmental Physics Laboratory, University of Vigo, Ourense, Spain

DANIEL M. MITCHELL

Department of Physics, University of Oxford, Oxford, and School of Geographical Science, University of Bristol, Bristol, United Kingdom

(Manuscript received 25 January 2017, in final form 2 October 2017)

ABSTRACT

The vertical coupling between the stratosphere and the mesosphere is diagnosed from polar cap temperatures averaged over 60°–90°N with a new method: the joint occurrence of a warm stratosphere at 10 hPa and a cold mesosphere at 0.01 hPa. The investigation of an 11-yr-long dataset (2004–15) from Aura-MLS observations shows that such mesospheric coupling days appear in 7% of the winter. During major sudden stratospheric warming events mesospheric couplings are present with an enhanced average daily frequency of 22%. This daily frequency changes from event to event but broadly results in five of seven major warmings being classified as mesospheric couplings (2006, 2008, 2009, 2010, and 2013). The observed fraction of mesospheric coupling events (71%) is compared with simulations of the Kühlungsborn Mechanistic Circulation Model (KMCM), the Hamburg Model of the Neutral and Ionized Atmosphere (HAMMONIA), and the Whole Atmosphere Community Climate Model (WACCM). The simulated fraction of mesospheric coupling events ranges between 57% and 94%, which fits the observations. In searching for causal relations weak evidence is found that major warming events with strong intensity or split vortices favor their coupling with the upper mesosphere. More evidence is found with a conceptual model: an effective vertical coupling between 10 and 0.01 hPa is provided by deep zonal-mean easterlies at 60°N, which are acting as a gravity-wave guide. The explained variance is above 40% in the four datasets, which indicates a near-realistic simulation of this process.

1. Introduction

Sudden stratospheric warming (SSW) events (Scherhag 1952; Matsuno 1971; Andrews et al. 1987) are strong atmospheric circulation anomalies influencing not only the troposphere (Baldwin and Dunkerton 1999; Sigmond et al. 2013; Mitchell et al. 2013) but also the mesosphere (Quiroz 1969; Labitzke 1972; Manney et al. 2008, 2009; Funke et al. 2010). A prominent feature is the cooling of the mesosphere, which occurs during the peak of the SSW event. Following the warming in the stratosphere, significant downward transport of thermospheric nitric oxide is reported with consequences for the reduction of stratospheric ozone (Bailey et al. 2014; Pérot et al. 2014). For some events, anomalies are found even in the ionosphere

Corresponding author: Christoph Zülicke, zuelicke@iap-kborn.de

DOI: 10.1175/JCLI-D-17-0047.1

(Goncharenko and Zhang 2008; Chau et al. 2009; Fuller-Rowell et al. 2010; Pedatella et al. 2014a,b). Many questions arise: How can such mesospheric anomalies be objectively diagnosed? How often are they observed? How well do numerical models simulate such phenomena? What are the relevant dynamical mechanisms?

Usually SSWs are classified according to stratospheric data, such as using the reversed zonal-mean meridional temperature gradient at 10 hPa for a "minor warming" or the reversed zonal-mean zonal wind at 60°N and 10 hPa for a "major warming" (Schoeberl 1978). Further categories refer to the split or displaced form of the polar vortex (Charlton and Polvani 2007) or to the duration of the events (Tomikawa 2010). Siskind et al. (2010) suggested referring to SSWs as "extended" when they show distinct mesospheric structures. They used the 2006 and 2008 Northern Hemisphere major SSWs to demonstrate features like a mesospheric cooling followed by the formation of an elevated stratopause elevated stratopause some days after the central date. The strong and long-lasting 2009 event also showed such structures (Manney et al. 2008, 2009; Funke et al. 2010; Chandran et al. 2014). Hitchcock and Shepherd (2013) characterized the evolution of the middle-atmosphere temperatures during the extended-time-scale recovery phase as polar-night jet oscillations (PJOs) (Kuroda and Kodera 2004). The diagnosis of both elevated stratopause and PJO phenomena requires a sophisticated diagnostic algorithm while a more simple approach would be an advantage. Beside a classification of the events in categories it should work on a daily basis and should also return a continuous index. The development of such a diagnostics is one aim of this paper.

The database for such a study has to cover the middle atmosphere with sufficient resolution. While operational atmospheric analyses include the troposphere and stratosphere, the mesosphere is treated with coarse vertical resolution only and is strongly damped. For example, the ECMWF Integrated Forecast System is set up with a level spacing of more than 2 km above 0.7 hPa and sponge layers starting at 10 and 1 hPa (ECMWF 2016, part III, pp. 14ff). Hence, global mesospheric data have to be derived from satellite measurements. In their study, Lee et al. (2009) used data from the Microwave Limb Sounder (MLS) aboard the sun-synchronous *Aura* satellite to obtain the vertical structure of the northern annular mode for the SSWs from 2005 until 2009. Their data covered the height region between 300 and 0.001 hPa and showed different evolutions of the mesospheric anomalies from year to year. Since then, Aura-MLS observations have continued and will be used here to quantify the stratosphere–mesosphere coupling.

Simulations with general circulation models have also shown vertically extended structures during SSWs (Liu and Roble 2002, 2005; Tomikawa et al. 2012; Limpasuvan et al. 2012; de la Torre et al. 2012; Zülicke and Becker 2013; Hitchcock and Shepherd 2013; Miller et al. 2013; Shepherd et al. 2014). Often, a strict anticorrelation between polar temperatures at 1 and 0.01 hPa was found as a common feature for the winter polar Northern Hemisphere (Karlsson et al. 2009; Tan et al. 2012), which may amplify during SSWs. This close relation between stratospheric warmings and mesospheric coolings in simulations will be compared with observational data.

Gravity waves (GWs) are mainly responsible for the link between the stratosphere and mesosphere (Holton 1982; Andrews et al. 1987): For normal winter conditions, the stratospheric wind is westerly and allows GWs with a westward phase speed to propagate into the mesosphere. There, they break and deposit their westward momentum, which induces a poleward and downward residual circulation. The corresponding dynamic warming supports the formation of the winter stratopause. During major warmings, the stratospheric wind changes to easterly directions, resulting in a dynamic cooling in the mesosphere. While this causal chain is well established, there are still uncertainties concerning details of the role of orographic and nonorographic GWs (referred to as OGWs and NGWs, respectively, in the following), their changing source intensities, and varying filter conditions. As shown by Ren et al. (2011) in simulations with the Whole Atmosphere Community Model (WACCM), parameterized NGWs appeared to be most important in driving the mesospheric circulation above 70 km altitude in the time following the central date. McLandress et al. (2013) confirmed such structures in CMAM simulations and noticed that OGWs and NGWs both play a role but do not simply superimpose. In simulations with GW-permitting resolution such as with the KANTO model (Watanabe et al. 2008; Tomikawa et al. 2012) or the Kühlungsborn Mechanistic Circulation Model (KMCM; Zülicke and Becker 2013), the characteristic structures were reproduced but not further differentiated for separate NGW and OGW influences. We aim to use the diagnosed mesospheric coolings to examine how far they are determined by the stratospheric wind filter effect. For this purpose, a conceptual GW propagation model with a fixed prescribed launch spectrum, as often applied in simple parameterizations of NGWs, will be developed and applied.

In the present paper we aim to diagnose the stratosphere–mesosphere coupling and to relate it to the dynamic mechanism. For this purpose a new diagnostic method and a conceptual model for GW propagation are developed, applied, and discussed. Data and methods are described in section 2. Using the new

diagnostics, observations are statistically analyzed and compared with simulations in section 3. There we also study the relevant physical process with the conceptual model. In section 4 we discuss the classification of vertical coupling, the representativity of observations, their coherence with simulations, and the physical interpretation of the results. In section 5 conclusions are drawn and an outlook is given. The appendixes contains technical details of the diagnostics and the conceptual model including a collection of definitions and formulas.

2. Data and methods

a. Data

For the study of the stratosphere–mesosphere coupling, we use daily satellite data and reanalyses as observations, and three well-documented model runs as simulations.

Observations from Aura-MLS are available from August 2004 until the present day as level 2 version 4 data (Livesey et al. 2015). The vertical resolution is 4 km in the stratosphere (10 hPa) but changes to 14 km at the mesopause level (0.01 hPa) and the precision of temperature increases from ±0.6 to ±3.3 K with altitude. For the analysis of the polar temperature, we use 60°–90°N area-weighted polar-cap average temperatures at levels between 260 and 0.001 hPa on a daily basis. Data until July 2015 are included in order to cover 11 complete years.

ERA-Interim reanalyses (referred to hereinafter as ERA; Dee et al. 2011) of zonal-mean zonal wind and geopotential height maps for the Northern Hemisphere are retrieved from the ECMWF archive with a resolution of 1.125° × 1.125° at 10 hPa as daily means from 6-hourly samples. The data selection covers the period from August 2004 until July 2015, according to the utilized satellite data.

A reference dataset on major warmings is compiled from the literature for verification purposes. From Table 1 in Tomikawa (2010) we take the central dates, duration, and maximum easterlies as derived from the Japanese 25-Year Reanalysis (JRA) and the Japan Meteorological Agency Climate Data Assimilation System. From Table 1 in Cohen and Jones (2011), which is the continued Charlton and Polvani (2007) analysis, the information on the vortex form (split or displaced) is taken as derived from NCEP–NCAR data. The event of 21 January 2006 is corrected to be a displacement (Hitchcock et al. 2013; Vignon and Mitchell 2015). To ensure the coherent selection of events we include only those which were identified in both datasets accepting deviations of the central dates of up to one day. These reference data cover the time period from 1979 to 2009.

Simulations of three mesosphere-resolving models are used: The KMCM (Becker 2009) is a spectral global circulation model. We use a permanent-January simulation of about 58 months with a spectral truncation at wavenumber 120 and 190 vertical levels (T120 L190) from the surface up to 120 km. This setup corresponds to a grid size of 170 km horizontally and about 600-m vertical level spacing up to about 100 km. The model allows for an explicit simulation of a significant part of the inertia and midfrequency GW spectrum to drive a realistic mesospheric circulation [see Zülicke and Becker (2013) for more information]. It further employs a temperature relaxation to an equilibrium state and a simple representation of latent heating (Körnich et al. 2006) in order to reproduce a climatological mean January state. Nonlinear interaction of Rossby waves and GWs with the mean flow leads to self-generated SSWs and associated mesospheric coolings. The first 21 months of the time series contained two major warmings, which were described in detail in Zülicke and Becker (2013). For the present study, the model run was prolonged with identical settings. This dataset is included in the present study as an example for a stationary mechanistic simulation of the general circulation on a time-invariant background field [i.e., without a seasonal cycle and quasi-biennial oscillation (QBO)] and resolved GWs that are mainly generated in the extratropical storm tracks (i.e., without any GW drag parameterization).

The Hamburg Model of the Neutral and Ionized Atmosphere (HAMMONIA; Schmidt et al. 2006) was used by Miller et al. (2013) to study SSWs. The model was run with a spectral truncation at wavenumber 31 and 67 vertical levels (T31 L67) with the uppermost layer centered at 1.7×10^{-7} (~250 km). This corresponds to a horizontal grid spacing of 3.75° × 3.75° and vertical layers of about 3-km thickness in the stratosphere. The time slice simulation used prescribed climatological sea surface temperatures, greenhouse gas concentrations representative of the 1990s, and solar irradiance typical for minimum conditions of the 11-yr cycle. OGWs are treated with the parameterization scheme of Lott and Miller (1997), and NGWs are parameterized following Hines (1997). The simulation contains self-induced SSWs but no QBO due to its relatively coarse vertical resolution. We include this 20-yr-long dataset in our study as an example for time slice simulations including a seasonal cycle and parameterized GWs.

SSWs were simulated with WACCM by de la Torre et al. (2012). This dataset was created with WACCM version 3.5.48 reaching up to 140-km height, a horizontal

resolution of about 210 km, and 66 vertical levels corresponding to about 3.5-km vertical resolution. WACCM contains a parameterization of GWs, turbulent mountain stress, and a prescribed QBO in the tropical regions (Richter et al. 2010). The model is further forced with observed sea surface temperatures, surface mixing ratios of greenhouse gases, and solar insolation corresponding to the period 1953–2006. This 54-yr-long time series is included as an example for a transient simulation including a seasonal cycle with parameterized GWs.

b. Methods

The data are analyzed in three steps to link mesospheric characteristics to stratospheric features. The interpretation of data is supported by the analysis of a conceptual model.

All data are resampled to daily means in order to make them comparable. Three of the datasets originally contain a diurnal cycle (ERA, HAMMONIA, and WACCM) while two do not (MLS and KMCM). From most of the data the daily mean eliminated tide signals that may become relevant in the mesosphere. The sun-synchronous MLS observations may still be biased by observing a specific phase of migrating tides. The high-latitude response of the migrating diurnal tide to major warmings, however, was found to be small (Pedatella et al. 2014b). The seasonal cycle is eliminated in the temperature deviations from the multiyear seasonal average as used for the mesospheric coupling diagnosis (Xu et al. 2009). The additional smoothing of the data over 3 days turns out to be effectively removing short-term and small-amplitude fluctuations, making the results more robust. This experience supports the inclusion of a smoothing procedure in an updated SSW definition (Butler et al. 2015).

The major warming diagnostics identifies events according to the criteria defined by Charlton and Polvani (2007) and Charlton-Perez and Polvani (2011): days from November to March with easterly 10-hPa zonal-mean zonal wind at 60°N are attributed to a major warming if the easterly wind period is preceded by at least 20 consecutive days of westerly wind and followed by at least 10 consecutive days of westerly wind before 30 April. Summary statistics of the major warming diagnostics are given in terms of the following quantities, which are defined in appendix A: the central day [t_{cen}, Eq. (A36): first day with easterly wind], duration [D, Eq. (A1): number of days with easterly wind], and maximum easterly wind [E_{max}, Eq. (A4)] for each event is obtained. The event intensity is defined as the accumulated easterlies [I_{acc}, Eq. (A15): sum of daily-mean easterly wind speed]. It serves as an integral measure combining information on amplitude and duration of the event. Additionally, a day-by-day table is obtained containing the label "major warming" (MW) for those days with easterly wind following the central date.

For the elliptic-vortex diagnostics, the algorithm described by Matthewman et al. (2009) and Mitchell et al. (2011) is used (see appendix B). In this study we analyze 10-hPa maps of geopotential height. The contour with the sharpest meridional gradient is chosen as the edge of the polar vortex. From the enclosed area, a number of weighted geometrical moments is calculated including a fitted ellipse. Following the recommendation of Seviour et al. (2013), the aspect ratio [$a > 2.5$, Eq. (B8): ratio of the major and minor axis of the fitted ellipse] is used to identify split vortices. Those days are labeled "split vortex" (SV); the others are labeled "displaced vortex" (DV).

The mesospheric coupling diagnostics identifies the 10-hPa warm-stratosphere and 0.01-hPa cold-mesosphere anomalies from 60°–90°N averaged polar-cap temperatures. An anomaly is defined for a deviation from the mean value that exceeds one standard deviation (the one-sigma range). The daily mean values and standard deviations are calculated from the combined year-to-year and seasonal average (see appendix C) taking into account interannual and intra-annual variations. Based on the diagnosed quantities we label a day as exhibiting mesospheric coupling (MC) if both a warm stratosphere (WS) and a cold mesosphere (CM) are detected. With that algorithm we diagnose warm stratosphere days that are coupled to the upper mesosphere.

A conceptual model for the GW propagation is used to study the dependence of the mesospheric zonal GW phase speed [c_{GW}, Eq. (D7)] on the stratospheric zonal wind fields (see appendix D). The GW launch spectrum includes phase speeds between -15 and $+15\,m\,s^{-1}$. Critical-level filtering in the stratosphere is taken into account for longitude and height dependent wind fields. The model-derived zonal-mean zonal GW phase speed in the mesosphere is taken as a proxy for dynamic heating: a positive (eastward) phase speed indicates dynamic cooling; a negative (westward) phase speed indicates dynamic warming. The theoretical justification for this relation is given in appendix E.

3. Results

a. Observations

The diagnostic methods are applied to datasets that cover the middle atmosphere. First, we present the analysis of daily ERA reanalyses and MLS satellite data and will refer to them as "observations." In the

TABLE 1. Features of observed major warming events as diagnosed from the ERA/MLS dataset. The columns indicate the major warming label, the central date (t_{cen}), duration (D), maximum easterly wind (E_{max}), and event intensity (I_{acc}). The intensity of the event is classified as strong or weak (SI or WI) with the threshold value of 50 m s^{-1} day^{-1}. Next, there is the near-event daily number and frequency of split vortices (n^*_{SV} and f^*_{SV}), where dSV denotes the number of split-vortex days. The corresponding vortex form is classified as split (SV) if there is at least one split-vortex day in the 21-day window ($f^*_{SV} > 0$); otherwise it is classified as displaced (DV, $f^*_{SV} = 0$). The number and frequency of mesospheric coupling days during the major warming event (n^*_{MC} and f^*_{MC}) are given in units of dMC (the number of mesospheric coupling days). The last column contains the corresponding coupling class: it is a mesospheric coupling event if there is at least one mesospheric coupling day in the 21-day window (MC; $f^*_{MC} > 0$), otherwise it is an uncoupled major warming event (UC; $f^*_{MC} = 0$).

MW label	T_{cen} (date)	D (days)	E_{max} (m s^{-1})	I_{acc} (m s^{-1} day)	Intensity	n^*_{SV} (dSV)	f^*_{SV} (dSV day^{-1})	Form	n^*_{MC} (dMC)	f^*_{MC} (dMC day^{-1})	Coupling
2006	21 Jan 2006	26	22.1	224	SI	0	0.00	DV	6	0.29	MC
2007	24 Feb 2007	4	5.2	11	WI	0	0.00	DV	0	0.00	UC
2008	22 Feb 2008	7	11.2	43	WI	0	0.00	DV	4	0.19	MC
2009	24 Jan 2009	30	26.7	316	SI	9	0.43	SV	7	0.33	MC
2010a	09 Feb 2010	3	3.5	7	WI	5	0.24	SV	4	0.19	MC
2010b	24 Mar 2010	3	2.1	4	WI	0	0.00	DV	0	0.00	UC
2013	7 Jan 2013	21	10.2	108	SI	4	0.19	SV	12	0.57	MC

following, the results will be detailed for the individual major warming events.

1) MAJOR WARMING CHARACTERISTICS

The characteristics of major warmings of the 3-day smoothed ERA data are shown in Table 1. Seven major warmings are found in the 11 winters between 2004/05 and 2014/15, which will be referred to as the 2006, 2007, 2008, 2009, 2010a, 2010b, and 2013 events. Zonal-mean zonal wind time series of these events at 60°N and 10 hPa are shown in Fig. 1. The strong intensity of the 2006 and 2009 events (Figs. 1a,d) is obvious. While processing the data we noticed that the duration of the 2006 and 2013 events (Figs. 1a,g) is sensitive to the particular choice of the sampling and averaging procedures. In both cases, a short phase with weak westerly winds would have artificially shortened the dominating easterly wind phase. This effect is accounted for by smoothing the data over 3 days.

A comparison of the central dates (t_{cen}; Table 1) with NCEP–NCAR data analyzed by Cohen and Jones (2011) reveals coincidence with maximum differences of 1 day, which can be attributed to the different datasets used. The 2010b event of 24 March 2010 is not in their table because it was probably too late, too short, and too weak for their analysis. Such differences could arise from details in the sampling and smoothing procedures. We find that all our central dates until 2010 are confirmed in the analysis of MERRA data from 1979 to 2011 by Hitchcock et al. (2013).

With regard to duration and maximum easterlies (D and E_{max}; Table 1), we compare our findings with Tomikawa (2010), who analyzed JRA data. For the duration we find agreement for the six overlapping events. One of his events (dated 14 Mar 2008) was not identified by us because there were only 14 days of westerly wind after the previous 2008 event (ending 28 Feb 2008). For the easterly-wind maximum the datasets agree well; differences are below 3 m s^{-1}.

With the present collection of major warming characteristics, we confirm the long and strong character of the 2009 and 2006 events and include the long 2013 event. Sorting the events according to descending values of the intensity (I_{acc}; Table 1), the ranking is 2009, 2006 and 2013. We empirically attribute strong intensity (SI) to those events exceeding 50 m s^{-1} day and weak intensity (WI) to the others. This threshold is oriented on the median of the seven observed intensities, which is 44 m s^{-1} day. As a result, the three abovementioned most intense events are classified as strong, which agrees with the classification in Kishore Kumar et al. (2014).

The statistics of major warming events are summarized in Table 2 (row ERA/MLS). The diagnosed frequency of major warmings [F_{MW}, Eq. (A6); Table 2] is 0.64 major warming events per year, only insignificantly larger than the reference number 0.6 given by Charlton and Polvani (2007). The event-averaged intensity [$\overline{I}_{acc}$, Eq. (A16); Table 2] is 102 m s^{-1} day, well above the threshold. Hence, the major warmings in our dataset are strong, on average. The number of three strong-intensity events [N_{SI}, Eq. (A20); Table 2] makes up a fraction [R_{SI}, Eq. (A31); Table 2] of 43%.

2) ELLIPTIC VORTICES

From the elliptic-vortex diagnostics of 10-hPa ERA-derived geopotential height maps, split vortices are found for the 2009, 2010a, and 2013 events. To characterize the time period near a certain event, we define 21-day windows ranging from 10 days before to 10 days after the central date. In these windows we find the number of near-event split-vortex days [n^*_{SV}, Eq. (A28); Table 1].

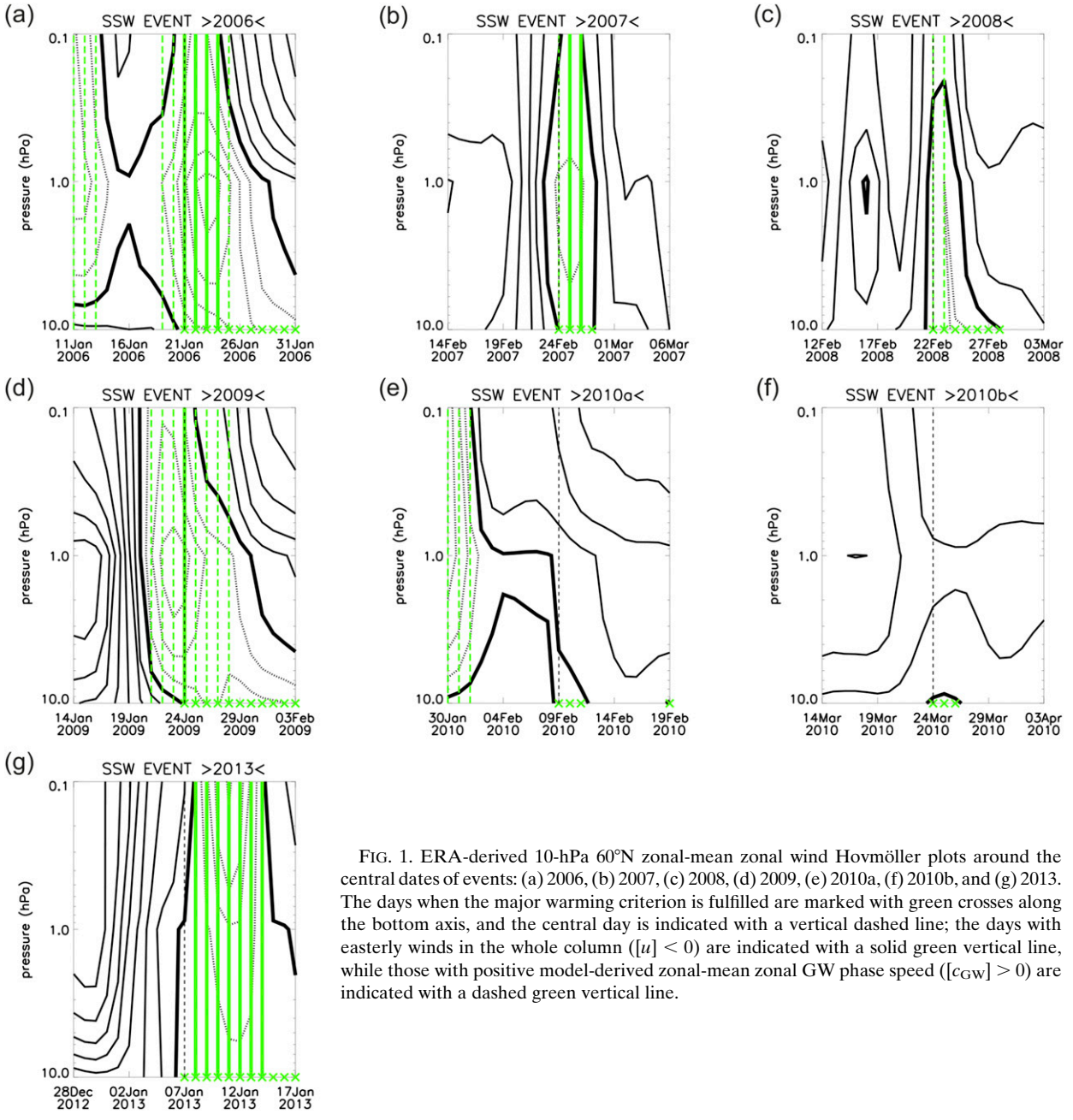

FIG. 1. ERA-derived 10-hPa 60°N zonal-mean zonal wind Hovmöller plots around the central dates of events: (a) 2006, (b) 2007, (c) 2008, (d) 2009, (e) 2010a, (f) 2010b, and (g) 2013. The days when the major warming criterion is fulfilled are marked with green crosses along the bottom axis, and the central day is indicated with a vertical dashed line; the days with easterly winds in the whole column ($[u] < 0$) are indicated with a solid green vertical line, while those with positive model-derived zonal-mean zonal GW phase speed ($[c_{GW}] > 0$) are indicated with a dashed green vertical line.

Taking the near-event frequency of them [f^*_{SV}, Eq. (A13); Table 1] we find numbers between 0 (no split-vortex days in the 21-day window) and 0.43 (43% of the days in the 21-day window show a split vortex). For a classification, we follow the formalism of Charlton and Polvani (2007) stipulating that the appearance of at least one split-vortex day around the central date is needed to term the whole event a "split-vortex event." In addition to this split/displaced classification (see the column labeled "form", Table 1) we provide with the frequency of split-vortex days (column f^*_{SV}, Table 1) a continuous measure for the form of the polar vortex.

Comparing the diagnosed vortex forms with the table in Cohen and Jones (2011) or Barriopedro and Calvo (2014), we find agreement for all but the 2006 event. Our efforts to resolve this issue are summarized as follows: When applying the algorithm to evaluate the vortex contours (Charlton and Polvani 2007) we do not find one day with a split vortex. Also with 10 other methods, combining the use of maps with Ertel's potential vorticity or absolute

TABLE 2. Statistics of major warming events. For the different datasets, their length (T), the number of major warming events and their frequency [N_{MW} and F_{MW}, where # denotes the number of major warming events] is given, the event-averaged duration ($\overline{D}$), maximum easterlies ($\overline{E}_{max}$), and intensity ($\overline{I}_{acc}$) as well as the number and fraction of strong-intensity events (N_{SI} and R_{SI}), split-vortex events (N_{SV} and R_{SV}), and mesospheric coupling events (N_{MC} and R_{MC}), with the standard error given in parentheses. For these indices, #SI denotes the number of strong-intensity events, #SV the number of split-vortex events and #MC the number of mesospheric-coupling events.

Data	T (yr)	N_{MW} (#MW)	F_{MW} (#MW yr^{-1})	$\overline{D}$ (days)	$\overline{E}_{max}$ (m s^{-1})	$\overline{I}_{acc}$ (m s^{-1} day^{-1})	N_{SI} (#SI)	R_{SI} (#SI/#MW)	N_{SV} (#SV)	R_{SV} (#SV/#MW)	N_{MC} (#MC)	R_{MC} (#MC/#MW)
ERA/MLS	11.0	7	0.64 (0.20)	13.4 (4.5)	11.6 (3.6)	102.3 (46.5)	3	0.43 (0.20)	3	0.43 (0.20)	5	0.71 (0.18)
KMCM	4.9	7	0.48 (0.17)	7.1 (1.2)	9.6 (2.8)	44.8 (16.9)	1	0.14 (0.14)	7	1.00 (0.00)	4	0.57 (0.20)
HAMMONIA	20.0	17	0.85 (0.17)	9.5 (2.0)	6.0 (1.4)	43.0 (14.2)	5	0.29 (0.11)	6	0.35 (0.12)	10	0.59 (0.12)
WACCM	54.0	32	0.59 (0.09)	7.0 (1.1)	6.9 (1.0)	41.4 (12.3)	6	0.19 (0.07)	6	0.19 (0.07)	30	0.94 (0.04)
JRA–NCEP	31.0	19	0.61 (0.10)	14.2 (2.7)	13.3 (1.8)				9	0.47 (0.12)		

vorticity with a split criterion using the kurtosis (Mitchell et al. 2011) or a wave 1/wave 2 projections, we do not detect split vortices between 19 January and 30 January 2006. Out of 11 methods four are successful in finding splits after 4 February 2006, but this is too late after the central date. The different methods give comparable results for the 2009 and 2013 events, while they depend on details of the data and methods for the others. We stay with our analysis, in line with the recommendation of Seviour et al. (2013), with using geopotential height maps and an aspect-ratio criterion. Consequently, the 2006 event is considered a displaced-vortex event. Agreement with our classification of vortex forms is found in Hitchcock et al. (2013) and Vignon and Mitchell (2015).

The major warming event statistics of vortex forms are summarized in Table 2 (row ERA/MLS). The three diagnosed split-vortex events [N_{SV}, Eq. (A21); Table 2] make up 43% of the major warmings [see R_{SV}, Eq. (A32); Table 2], which compares well with the findings of Charlton and Polvani (2007).

The daily statistics of split vortices are given in Table 3 (row ERA/MLS). A total of 70 split-vortex days has been found in the time series [n_{SV}, Eq. (A26); Table 3]. The comparison with the event-accumulated number of split-vortex days [$\hat{n}^*_{SV}$, Eq. (A29): sum of mesospheric-coupling days in 21-day windows around major warming central dates; Table 3] reveals that about one-fourth of the split-vortex days (18 of 70) appear near the major warming events. Accordingly, their event-averaged frequency [$\overline{f}^*_{SV}$, Eq. (A14); Table 3] is about 4 times larger than the total frequency [f_{SV}, Eq. (A11); Table 3]. Both numbers clearly indicate that they play an important but not exclusive role in the SSW-related circulation changes.

3) MESOSPHERIC COUPLINGS

Before the results of the mesospheric coupling diagnostics are presented we analyze temperature profiles. The MLS-derived daily temperature deviations from the multiyear mean values [defined in Eq. (C2)] are used to calculate the profiles shown in Fig. 2. The average profile for the whole winter (November–March) is shown with a black line including the 95% significance ranges estimated with a Student's t test and an effective degree of freedom according to Zülicke and Peters (2010). In Fig. 2a, significant warm anomalies in the stratosphere and cold anomalies in the mesosphere are seen in the means over 21-day windows around each event (colored lines). Figure 2b shows higher daily variance during winter at about 1 hPa, while for the majority of major warming events a distinct peak in the stratosphere is found between 10 and 1 hPa. To stay with the historically established analyses we select 10 hPa for the stratospheric data. In the mesosphere, nearly all major warming events show variances above the winter average at 0.1 and 0.001 hPa. Linear correlation coefficients with respect to the 10-hPa level are shown in Fig. 2c. For the whole wintertime series we note positive correlations ($r > 0.5$) between 40 and 2 hPa and negative correlations ($r < -0.5$) between 0.2 and 0.007 hPa. Hence, the mesospheric temperatures are usually anticorrelated to the stratosphere. Correlation profiles for each event are calculated from 21-day windows. While the anticorrelation around 0.2 and 0.1 hPa is robust for all major warming events, the correlations at 0.01 hPa show some variation: while 5 of 7 events are anticorrelated, 2 of 7 are uncorrelated. These two events (2007 and 2010b) show only weak variance in Fig. 2a. Further above, the variances for the strong events decrease and they become uncorrelated. Hence, for the discrimination between events with different impact on the upper mesosphere the 0.01-hPa level is suitable.

The result of the mesospheric coupling diagnostics is shown with time series of polar cap temperatures for the stratosphere at 10 hPa and for the mesosphere at 0.01 hPa in Fig. 3. The mean and the one-sigma range are occasionally widened by strong warmings during late winter. Such features can be noted for January as a consequence of the 2006 and 2009 events. However, the seasonal smoothing is sufficient to allow for a detection of the subseasonal anomalies associated with stratospheric warmings. During all winter days (i.e., from November

TABLE 3. Daily statistics of split vortices and mesospheric couplings in winter. For the number of winter days (T_+), the number and frequency of split-vortex days (n^+_{SV} and f^+_{SV}) are given together with the event-accumulated number and event-averaged frequency ($\hat{n}^*_{SV}$ and $\bar{f}^*_{SV}$). Correspondingly, there is given the number and frequency of winter mesospheric coupling days (n^+_{MC} and f^+_{MC}) with their event-accumulated number and event-averaged frequency ($\hat{n}^*_{MC}$ and $\bar{f}^*_{MC}$).

Data	T_+ (days)	n^+_{SV} (dSV)	f^+_{SV} (dSV day^{-1})	$\hat{n}^*_{SV}$ (dSV)	$\bar{f}^*_{SV}$ (dSV day^{-1})	n^+_{MC} (dMC)	f^+_{MC} (dMC day^{-1})	$\hat{n}^*_{MC}$ (dMC)	$\bar{f}^*_{MC}$ (dMC day^{-1})
ERA/MLS	1645	70	0.04	18	0.12	114	0.07	33	0.22
KMCM	1787	212	0.12	74	0.50	137	0.08	42	0.29
HAMMONIA	3025	95	0.03	27	0.08	175	0.06	57	0.17
WACCM	8094	107	0.01	54	0.08	742	0.09	216	0.32

through March), we count 278 days with a warm stratosphere and 209 days with a cold mesosphere. Both features appear together at 114 days as mesospheric couplings [n^+_{MC}, Eq. (A23); Table 3].

Is there a connection to the mesosphere during major warmings? For the analysis of this question, we derive the number and frequency of mesospheric coupling days near major warming events [n^*_{MC} and f^*_{MC}, Eqs. (A24) and (A9); Table 1]. Usually they appear in the time window from 5 days before to 10 days after the central date. Only for the 2010a event (centered at 9 February 2010) is there a sequence of mesospheric coupling days from 26 January until 2 February 2010, ending just 6 days before the central date (see Fig. 3f). To include them, we begin the time window for the near-event analysis 10 days before the central date and end it 10 days after the central date. Using this definition, we find the near-event mesospheric coupling frequency to be different from event to event ranging from 0 to 0.60 mesospheric-coupling days per day (dMC day^{-1}) (f^*_{MC}; Table 1). Accepting at least 1 mesospheric coupling day in this 21-day window ($f^*_{MC} > 0$) to classify the event a mesospheric coupling, we find 5 of such events [N_{MC}, Eq. (A18); Table 2] in 11 years of data. Using these categories, a fraction of more than two-thirds (71%) of the major warming events can be classified as mesospheric couplings [R_{MC}, Eq. (A30); Table 2].

As mentioned above, mesospheric coupling days are not only found during major warmings. Of the total-winter number of mesospheric coupling days [n^+_{MC}, Eq. (A25), Table 3, row ERA/MLS] we find only 29 % near the major warming events [see the event-accumulated number of mesospheric-coupling days, n^*_{MC}, Eq. (A25), Table 3, row ERA/MLS]. Accordingly, their daily frequency (0.22) is clearly enhanced around major warmings by a factor of 3 [cf. the near-event and total-winter frequencies $\bar{f}^*_{MC}$ and f^+_{MC}, Eqs. (A10) and (A8); Table 3]. During major warmings, on average every fifth day is subject to a coincident cold upper mesosphere.

4) STATISTICAL ANALYSIS

A statistical analysis is performed in order to identify stratospheric conditions that lead to a cooling in the upper mesosphere. In a first attempt in this search for causal relations, the major warming features estimated from 10-hPa data are used. We may expect that the

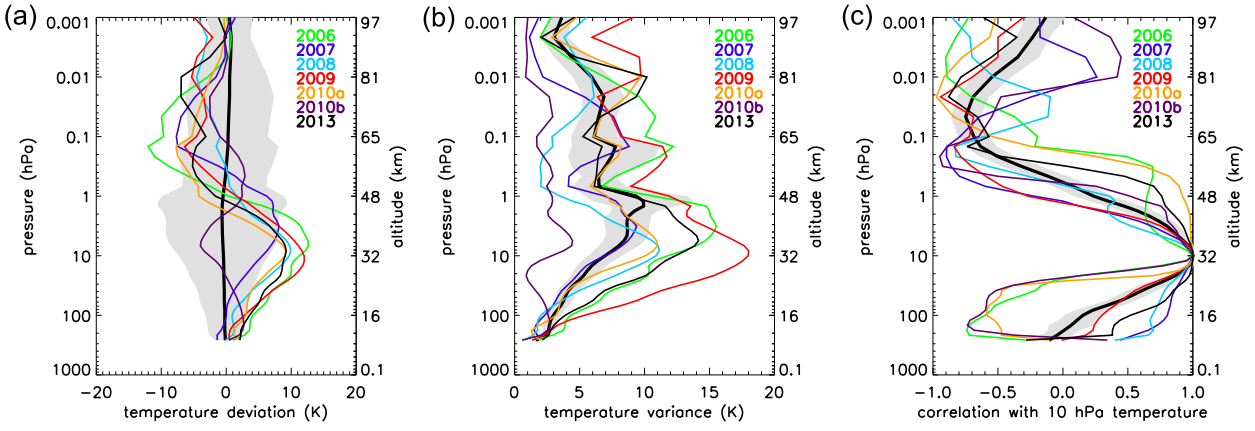

FIG. 2. MLS-derived profiles of 60°–90°N polar-cap temperature anomaly (a) mean, (b) variance, and (c) correlation with that at the 10-hPa level. The profiles for all winter days are shown with a thick black line including the 95% significance range. The thin colored lines are the results for 21-day windows around the central dates of the major warming events 2006, 2007, 2008, 2009, 2010a, 2010b, and 2013.

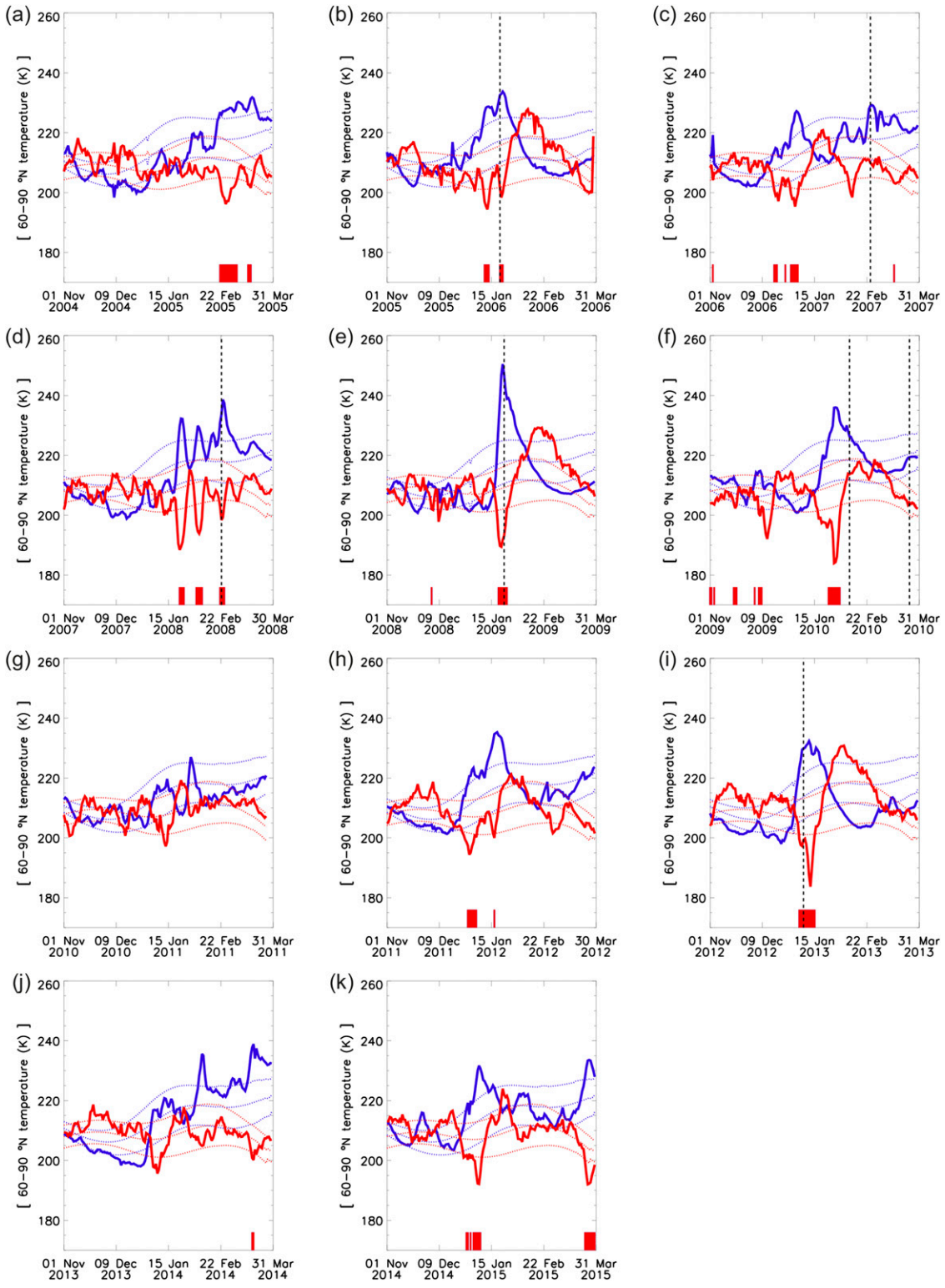

FIG. 3. MLS-derived 60°–90°N polar-cap temperature time series at 10 hPa (blue) and 0.01 hPa (red) for (a) 2004/05, (b) 2005/06, (c) 2006/07, (d) 2007/08, (e) 2008/09, (f) 2009/10, (g) 2010/11, (h) 2011/12, (i) 2012/13, (j) 2013/14, and (k) 2014/2015 showing the raw temperature (solid) and the one-sigma range around the interannual mean (dotted). Mesospheric coupling days are marked with a red tick along the bottom axis. The central dates of major warmings are indicated with vertical dashed lines.

TABLE 4. Correlations between near-event frequency of mesospheric couplings and event intensity (r_{MC-SI}: f^*_{MC} vs I_{acc}), frequency of split vortices (r_{MC-SV}: f^*_{MC} vs f^*_{SV}), and 21-day mean model-derived zonal-mean GW phase speed (r_{MC-GW}: f^*_{MC} vs c^*_{GW}). The related standard error is given in parentheses.

Data	r_{MC-SI}	r_{MC-SV}	r_{MC-GW}
ERA/MLS	0.55 (0.32)	0.52 (0.32)	0.66 (0.28)
KMCM	−0.06 (0.38)	0.45 (0.34)	0.75 (0.25)
HAMMONIA	0.52 (0.21)	0.26 (0.23)	0.63 (0.19)
WACCM	0.20 (0.17)	0.26 (0.17)	0.65 (0.13)

stronger the major warmings, the more frequently they couple to the mesosphere, and vice versa (hereafter referred to as the strong/coupled hypothesis). With reference to Table 1, the near-event frequency of mesospheric couplings is related to the event intensity (f^*_{MC} vs I_{acc}). The linear correlation coefficient of 0.55 indicates 30% explained variance (see Table 4, row ERA/MLS, column r_{MC-SI}). Taking the classification for intensity (WI or SI) and coupling (MW or MC) from Table 1, we find the strong major warming events of 2006, 2009, and 2013 all appear to be associated with mesospheric couplings, whereas the weak 2007 and 2010b events do not show mesospheric couplings. Thus, 5 of 7 events follow the hypothesis. The 2008 and 2010a events are weak but coupled and thus 2 of 7 events do not follow the hypothesis. It is interesting to note that for strong major warmings the frequency of mesospheric couplings is above 0.29 per day (see SI intensity and f^*_{MC} in Table 1).

Another attempt is made for the mesospheric coupling frequency versus the split-vortex frequency (not shown) to test the split/coupled hypothesis: the more frequently split vortices occur, the more frequent are the mesospheric couplings (f^*_{MC} vs f^*_{SV}). The correlation also reveals an explained variance of 24% (see Table 4, row ERA/MLS, column r_{MC-SV}). With reference to the classification of the vortex form (SV or DV; Table 1, column form), we find that three splitting events are associated with a mesospheric coupling (2009, 2010a, and 2013) whereas two displacement events are not (2007 and 2010b). These 5 of 7 events follow the split/coupled hypothesis. Two events are displacements but are of the mesospheric coupling class (2006 and 2008) and so they violate the hypothesis. Hence, the split/coupled hypothesis does not explain more variability than the strong/coupled hypothesis.

As the analysis of indices calculated from 10 hPa data alone does not allow for a clear identification of mesospheric couplings, we further investigate profiles extending over several levels. From the 21-day windows around the major warming events, we form zonal-mean zonal wind composites of those days with a mesospheric coupling and those without, at three selected levels (10, 1, and 0.1 hPa). Figure 4a clearly shows a difference in these profiles. The mesospheric couplings seem to be associated with mainly easterly wind through the stratosphere. We take this as a hint as to a link between deep easterlies and mesospheric couplings (the deep/coupled hypothesis).

5) CONCEPTUAL MODEL

In this section, we relate the deep/coupled hypothesis to a physical process. With a conceptual model we follow the propagation of GWs through three levels of a horizontally and vertically varying stratospheric zonal wind field. The model, detailed in appendix D, is solved numerically.

It is instructive to consider an analytical solution for a special case. For a height-independent and longitude-independent zonal wind, the model-derived zonal GW phase speed is shown in Fig. 5 as a solid line. It is eastward (positive) for sufficiently easterly (negative) wind, while it is westward (negative) for sufficiently westerly (positive) wind. If the wind is varying with height, its minimum and maximum values determine the transmission properties with respect to GWs. Such a case is visualized by the dashed line for a minimum zonal wind $u_{min} = -10\,m\,s^{-1}$ and a maximum wind indicated by the value of the x axis. The phase speed stays constant at $10\,m\,s^{-1}$ for maximum zonal winds between -10 and $0\,m\,s^{-1}$ because no additional GW filtering occurs compared to the constant $10\,m\,s^{-1}$ wind profile. When the maximum wind speed is increased to positive values, additional filtering of GWs with westerly phase speeds occur and the GW phase speed decreases. Zero phase speed is reached for a critical zonal wind of $10\,m\,s^{-1}$ [see Eq. (D9)].

Inspecting observed wind profiles for deep zonal-mean easterlies ($[u] < 0$ at 10, 1, and 0.1 hPa, where the brackets [...] indicate the zonal mean) we identify such days with solid green lines in Fig. 1. Such occasions for maximum dynamic cooling are found for the major warming events of 2006, 2007, 2009, and 2013. Relaxing the zonal-wind requirements for some dynamic cooling ($[c_{GW}] > 0$ at 0.01 hPa), which allows for weak westerlies, we find considerably more occasions, which are indicated with dashed green lines. These appear for all events but 2010b.

Time series of the model-derived zonal-mean zonal GW phase speed are shown in Fig. 6. SSW-related phases with eastward GWs (positive phase speed) are found for all events but 2010b. Their appearance depends not only on the 10-hPa zonal-mean zonal wind but is a joint effect of all three levels. For example, for the 2009 event (Fig. 6d) the 10-hPa wind changes to east a couple of days after the winds at 1 and 0.1 hPa. As a consequence of the time shift in the behavior of the winds, the phase speed is peaking before the 10-hPa easterlies reach their maximum. For most of the events

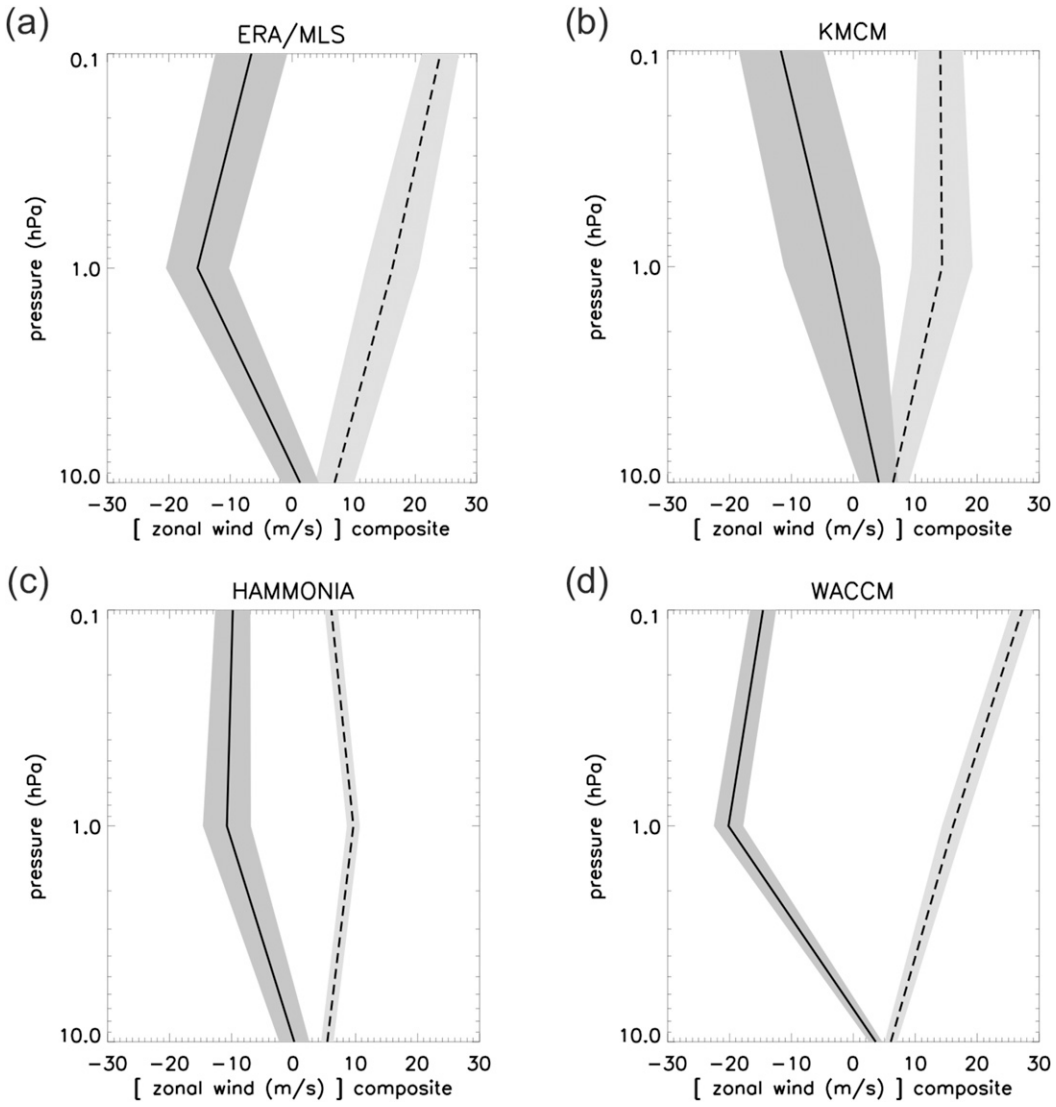

FIG. 4. Zonal-mean zonal wind composites of near-event mesospheric coupling days (solid) and uncoupled days (dashed) with the 95% significance range (gray shaded) for (a) ERA/MLS, (b) KMCM, (c) HAMMONIA, and (d) WACCM.

(2006, 2008, 2009, 2010a, and 2013) each phase with positive phase speed (green ticks at upper axis) is accompanied by a mesospheric coupling (red ticks at lower axis). For 2010b the phase speed remains negative all the time, and accordingly there is no significant mesospheric cooling. The only exception from the deep/coupled relation is the 2007 event, when the coupling is missing although the phase speed is positive. Hence, the inspection of time series suggests that deep easterlies extending from 10 to 0.1 hPa support mesospheric coolings. The timing of coupling with respect to the central day is quite variable. It is also interesting to note that the appearance of zonal-mean deep easterlies is not directly associated to the zonal-wave split-vortex form. The vortex-displacement deep-easterly events 2006 and 2008 are counterexamples.

Next we show in Figs. 7a and 7b the relation between the model-derived zonal-mean zonal GW phase speed and the observed mesospheric coolings (negative temperatures anomalies). Data are shown for the near-event day with the coldest anomaly. Note that the climatological reference state is in the lower-left corner, which is associated with zero temperature anomaly and most negative phase speed resulting from strong positive (westerly) zonal wind. Using 10-hPa wind for the phase speed estimates (Fig. 7a), these data suggest a correlation of 0.46. Including the 1- and 0.1-hPa levels (Fig. 7b), an enhanced correlation of 0.95 is found.

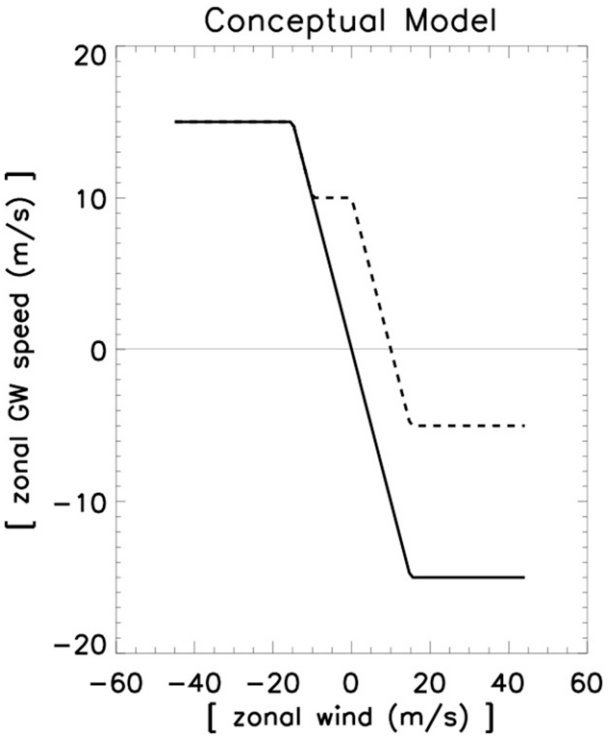

FIG. 5. Model-derived zonal-mean zonal GW phase speed dependence on the zonal-mean zonal wind. The solid line is for a uniform wind profile; the dashed line is for a profile with a minimum wind of $-10\,\mathrm{m\,s^{-1}}$ and a maximum wind on the x axis according to Eq. (D8).

The model-derived zonal-mean zonal GW phase speed also correlates with the frequency of mesospheric couplings (see Figs. 7c,d). In this plot the climatological reference state is the lower-left corner (no mesospheric coupling, most negative phase speed, strong positive zonal wind). To show the influence of data selection, we take the mean over a 21-day window around the central dates and find a correlation coefficient of 0.45 for the one-level estimate (Fig. 7c) and 0.66 for the three-level estimate (Fig. 7d). Both datasets (Figs. 7b,d) indicate an influence of deep easterlies on mesospheric couplings.

Without further documentation we add here a note on the impact of planetary wave structures. To conceptually model such height-dependent and longitude-dependent wind fields, we first calculate the GW propagation at every longitude and then take the zonal mean over the mesospheric GW phase speed. From studies with synthetic stratospheric zonal wind fields we find that large amplitudes and high vertical wavenumbers reduce the zonal-mean mesospheric zonal GW phase speed and associated dynamic heating. However, when including zonally asymmetric zonal winds from the observations no significant improvement of the predicted mesospheric couplings was found. This implies that the impact of the zonal-mean zonal wind profiles on zonal-mean GWs is dominant in the observations.

b. Simulations

After the analysis of observations we next diagnose model simulations with the same methods as used for the observations.

1) KMCM SIMULATIONS

Seven major warmings are found in the KMCM data (N_{MW}; Table 2, row KMCM). The number of major warmings per January month from this prolonged dataset (0.12) is nearly the same as reported in Zülicke and Becker (2013) for the first part of the time series (0.11). Wave-2 patterns of the polar vortex were identified, which is confirmed by the present analysis, which classifies all seven events as splittings. The frequency of the major warming events (F_{MW}; Table 2) is calculated from the number of events per January month. Assuming the same frequency for all four winter months (November–February) results in an estimate of 0.48 major warming events per year. The characterization of four events as mesospheric couplings (N_{MC}; Table 2) also corresponds to Zülicke and Becker (2013), where the joint appearance of a warm stratosphere with a cold mesosphere was found to be a rule of thumb (cf. their Fig. 8a with our Fig. 2b).

The daily statistics of the SSW features (see Table 3, row KMCM) reveal that the frequency of splits is about 4 times higher during major warmings (cf. f^{+}_{SV} with $\overline{f}^{*}_{\mathrm{SV}}$ in Table 3). A similar ratio is deduced from the frequency of mesospheric couplings (cf. f^{+}_{MC} with $\overline{f}^{*}_{\mathrm{MC}}$ in Table 3).

From the analysis of classifications (not shown) we find that 2 of 7 events follow the relation between strong intensity and mesospheric coupling. The simulation has strong variability in the frequency of mesospheric coupling days but small variation in the event intensity (not shown). As a consequence, the related correlation coefficient (see Table 4, where row KMCM, column $r_{\mathrm{MC–SI}}$ has an insignificant value. The correlations to the split-vortex frequency (column $r_{\mathrm{MC–SV}}$) and the GW phase speed are clearly higher (column $r_{\mathrm{MC–GW}}$). This behavior is a consequence of the relatively weak intensity of the simulated major warmings and the frequent appearance of split vortices (see R_{SI} and R_{SV} in Table 2, row KMCM).

2) HAMMONIA SIMULATIONS

17 major warmings are identified in the 20-yr-long simulation with HAMMONIA (N_{MW}; Table 2, row HAMMONIA). An event-by-event comparison with Miller et al. (2013) revealed coincidence for all but two cases. The first case was before the beginning of the

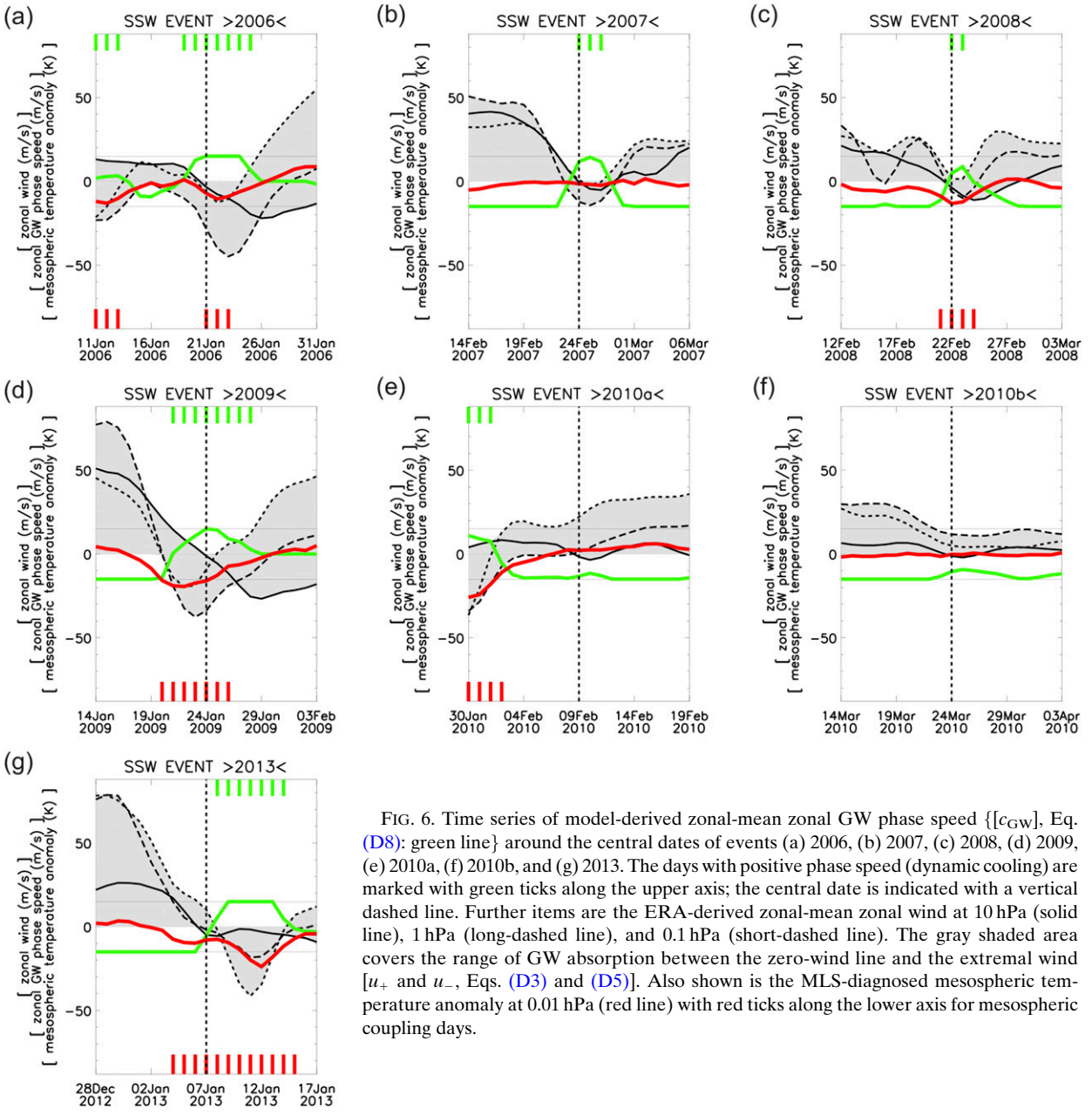

FIG. 6. Time series of model-derived zonal-mean zonal GW phase speed {$[c_{GW}]$, Eq. (D8): green line} around the central dates of events (a) 2006, (b) 2007, (c) 2008, (d) 2009, (e) 2010a, (f) 2010b, and (g) 2013. The days with positive phase speed (dynamic cooling) are marked with green ticks along the upper axis; the central date is indicated with a vertical dashed line. Further items are the ERA-derived zonal-mean zonal wind at 10 hPa (solid line), 1 hPa (long-dashed line), and 0.1 hPa (short-dashed line). The gray shaded area covers the range of GW absorption between the zero-wind line and the extremal wind [u_+ and u_-, Eqs. (D3) and (D5)]. Also shown is the MLS-diagnosed mesospheric temperature anomaly at 0.01 hPa (red line) with red ticks along the lower axis for mesospheric coupling days.

dataset analyzed by us, and the second case was a weak-wind and late-winter event that was eliminated by our 3-day smoother. Consequently, our major warming event frequency (F_{MW}; Table 2) is smaller than theirs [0.95 major warming events per year (#MW yr^{-1})]. Another value to compare is the ratio of displacement to splitting events [which is $1/(R_{SV}-1) = 1.8$ with Table 2]. Miller et al. (2013) calculated a ratio of only 1.1 but used a minimum finder to diagnose the vortex form.

The daily statistics in Table 3 (row HAMMONIA) reveal that the frequency of split-vortex days is about 3 times higher during major warmings (cf. $\overline{f}^*_{SV}$ with f^+_{SV} in Table 3). An increase by the factor of 3 is found for the frequency of mesospheric coupling days (cf. $\overline{f}^*_{MC}$ with f^+_{MC} in Table 3).

In the HAMMONIA data we find a clear event-to-event variability. While the events with strongest intensity and highest splitting frequency also show mesospheric coupling signatures, there are also cases deviating from the expected relation. For the major warming classification, we find 10 of 17 events following the hypothesized relation between strong intensity and

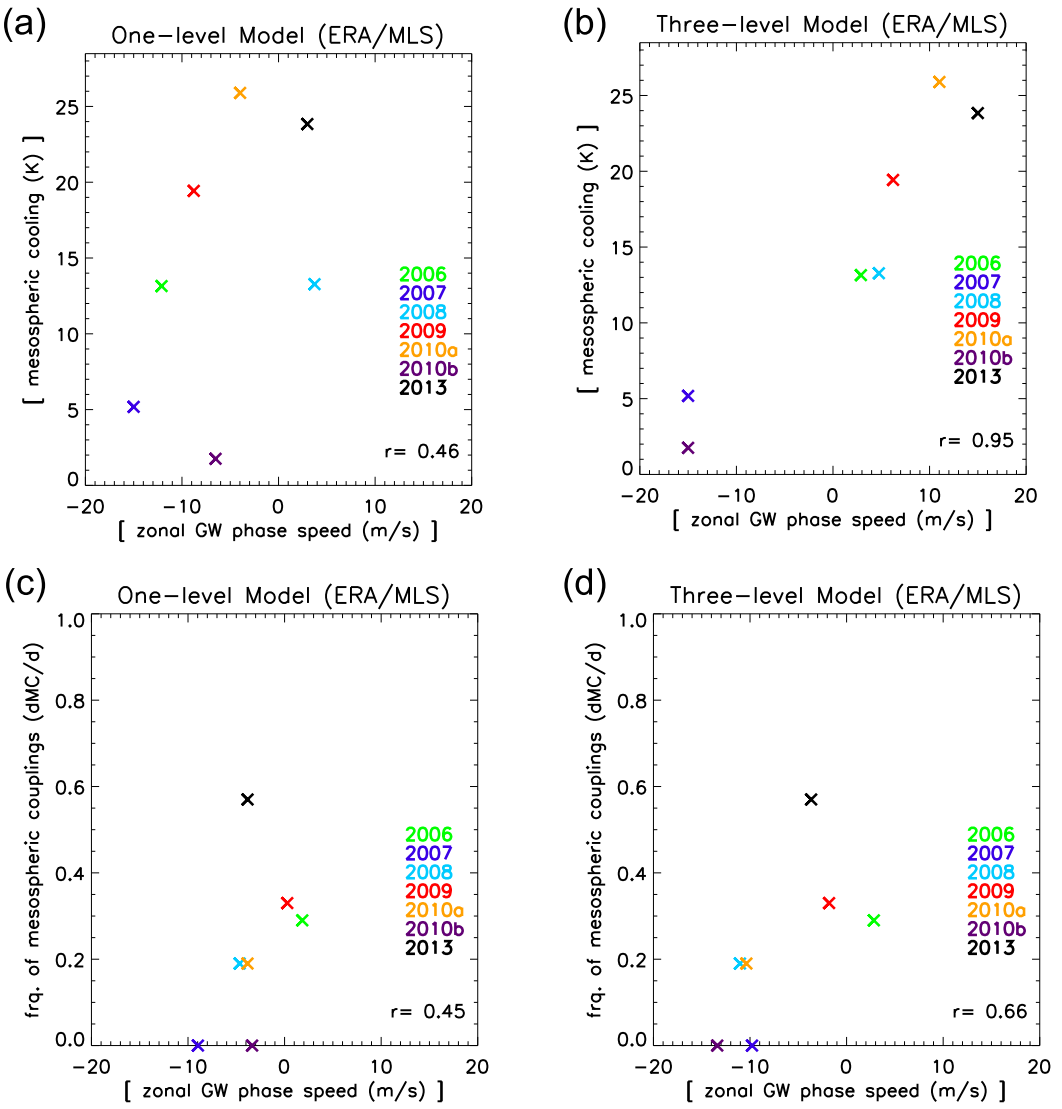

FIG. 7. Scatterplot of MLS-diagnosed (a),(b) mesospheric coolings (negative temperature anomalies) for the near-event coldest-anomaly day and (c),(d) frequency of mesospheric couplings (f^*_{MC}) for the near-event 21-day mean vs model-derived zonal-mean zonal GW phase speed ($[c_{GW}]$) based on ERA-derived zonal-mean zonal winds from (a),(c) one level (10 hPa) or (b),(d) three levels (10, 1, and 0.1 hPa). The correlation coefficient is given in the lower-right corner.

mesospheric coupling. The correlations compiled in Table 4 (row HAMMONIA) are all statistically significant. The highest correlation is found for the mesospheric coupling frequency versus GW phase speed (column $r_{MC–GW}$).

3) WACCM SIMULATIONS

In the 54-yr-long WACCM simulation we diagnose 32 major warming events (N_{MW}; Table 2, row WACCM). In comparison with de la Torre et al. (2012), we find exact daywise agreement of the central dates except for two cases. Differences are traced back to easterly wind periods that follow the preceding events too closely (less than consecutive 20 days of westerlies between). The split-vortex events (N_{SV}; Table 2) were less numerous than reported by them (16). However, in contrast to us they used a subjective classification method. Nearly all of the major warming events are accompanied with mesospheric couplings (see R_{MC} in Table 2).

The daily statistics (Table 3, row WACCM) indicate from a comparison of total and event-averaged frequencies that split-vortex days appear 8 times more frequently (see $\bar{f}^*_{SV}/f^+_{SV}$ in Table 3) and mesospheric couplings 4 times more frequently (see $\bar{f}^*_{MC}/f^+_{MC}$ in Table 3) during major warming events.

A high variance is found in the mesospheric coupling frequency but lower variance in the event intensity. From the classification, we find 8 of 32 events following the strong-intensity–mesospheric coupling link. The indices explain between 4% and 42% of variance (see Table 4, row WACCM, from columns $r_{MC–SI}$ to $r_{MC–GW}$).

4. Discussion

a. Classification of vertical coupling

A new algorithm for the objective identification of vertically extended SSWs is proposed with the mesospheric coupling diagnostics. For the detection of daily anomalies, such as an anomalously warm stratosphere or cold mesosphere, it is necessary to find the time-dependent mean and variance from the available data. With the applied procedure we include the year-to-year and seasonal variability. At both stratospheric and mesospheric levels (see Fig. 3) an increased variance is seen during wintertime (see the dotted lines for mean and one-sigma range). A fraction of these changes in sigma is the effect of strong SSW events around middle January and late February, as a visual inspection suggests. This is the time period with most SSWs (Charlton and Polvani 2007) accompanied with strong variability in the mesosphere. However, the chosen one-sigma criterion is sufficiently stable for the detection of temperature anomalies in the middle atmosphere in datasets with differing variability.

The daily statistics of mesospheric couplings reveal their relative high frequency. So we find several mesospheric coupling days that are not associated with stratospheric easterlies. Such events could be considered as minor warmings. During major warming events the frequency of mesospheric couplings appears to be increased. For the further analysis, we focus on the analysis of major warming events to stay compatible with previous studies.

With the suggested classification of mesospheric coupling events we may compare our results with the elevated-stratopause classification. For this purpose we attribute the considered major warming events to years, which reveals the mesospheric coupling events in 2006, 2008, 2009, 2010, and 2013 (see Table 5). All these years but 2008 were also subject to elevated-stratopause events as documented in Chandran et al. (2014). In these cases, the simultaneous appearance of a cold mesosphere and warm stratosphere was followed by the reformation of a warm mesosphere some days later. Hitchcock et al. (2013) diagnosed PJO events from MERRA and MLS for the years 2006, 2009, and 2010; we have added 2013 as another PJO based on our own analysis. All these years also showed mesospheric couplings and elevated stratopauses. The strong SSW events of 2006, 2009, and 2013 were additionally associated with enhanced downward transport during the recovery phase (Orsolini et al. 2010; Pérot et al. 2014). During the weaker event of 2010 the split-vortex form supported the formation of an elevated stratopause and PJO.

TABLE 5. Classes of observed major warmings. For each winter it is noted if the event was of a strong-intensity (SI), split-vortex (SV), or mesospheric-coupling (MC) class as defined for Table 1. Further, it is added if the event was found to be associated with an elevated stratopause (ES) or a polar-night jet oscillation (PJO) or if a strong descent (SD) from thermosphere to mesosphere has been observed.

Winter	SI	SV	MC	ES	PJO	SD
2006	SI		MC	ES	PJO	SD
2007						
2008			MC			
2009	SI	SV	MC	ES	PJO	SD
2010		SV	MC	ES	PJO	
2013	SI	SV	MC	ES	PJO	SD

Overall, the diagnosed SSW features complement each other well, characterizing different phases of the SSW life cycle. Like the two-level mesospheric coupling algorithm, the profile-based PJO analysis identifies the initial and central phase of the SSW with a warm stratosphere and a cold mesosphere in their principal component 1 (PC1) [see Fig. 2 in Hitchcock et al. (2013), with a positive temperature anomaly at 1 hPa and a negative anomaly at 0.01 hPa]. The elevated-stratopause algorithm follows the old subducted and the new elevated stratopauses during the recovery phase of the SSW, which corresponds to the transition to principal component 2 (PC2) of the PJO analysis (identifying positive temperature anomalies at 10 hPa and negative anomalies between 1 and 0.1 hPa, supplemented with a nearly neutral temperature between 0.01 and 0.001 hPa). This is similar to a downward-shifted PC1 with a lowered old stratopause and an elevated new one. The different phases of the SSW evolution are closely linked though subject to different physical driving. While the changes of the stratospheric wind from west to east imply changes in the propagation conditions for GWs, leading to a breakdown of dynamic heating in the mesosphere within a few days, the return to winter with stratospheric westerlies leads to enhanced dynamic heating through downwelling during a more extended time. This depends not only on the strength of the perturbation during the peak of the SSW but also on the seasonal and planetary-scale state of the atmosphere. Hence, detection of mesospheric couplings and PJO/PC1 features in the initial and peak phase of strong

SSWs is closely linked to the appearance of an elevated stratopause, strong descent, and PJO/PC2 in the recovery phase.

b. Representativity of observations

In this section the results from the observations are discussed. We consider the representativity of the diagnosed quantities and their use for a comparison with model simulations.

The frequency of major warming events during 2004–15 is diagnosed from analyses (F_{MW}; Table 2, row ERA/MLS) and found to be larger than the climatological reference value provided by Charlton and Polvani (2007). This difference, however, is insignificant [a Student's t test for difference of means with different standard deviations and sample sizes as in von Storch and Zwiers (2003), section 6.6.5, returns 17%]. To further evaluate the representativity of our major warming frequency we compile SSWs from another long-term dataset that is similar to the climatology (F_{MW}; Table 2, row JRA–NCEP). The additional agreement of our value of 0.64 major warmings per year (F_{MW}; Table 2, row ERA/MLS) suggests its representativity for the long-term mean. Although there are indications of enhanced stratospheric variability due to climate change (McLandress and Shepherd 2009; Gerber et al. 2010) and climate variability (Reichler et al. 2012), our dataset is not long enough to address these issues. We include the uncertainty of the estimates due to the limited database in Table 2 with the standard error in brackets. The error range of F_{MW} for 70% significance is from 0.44 to 0.84 MW yr^{-1}.

The issue of the limited size of our dataset is discussed with the standard error of the frequency of major warming events. From the value (e) of 0.1 #MW yr^{-1} given by Charlton and Polvani (2007) we infer with 23 MWs (n) a standard deviation ($s = e\sqrt{n}$) of 0.53 #MW yr^{-1}. From our dataset we obtain with a standard error $e = 0.2$ MW yr^{-1} and a sample size $n = 7$ MWs the same standard deviation s (i.e., the physical variability in both datasets does not differ). Hence, with a 4 times longer dataset we would end up with the same standard error as indicated in the commonly accepted reference number.

The characteristics of observed SSW events are summarized in Table 1. Such a summary updates and extends published information in several respects. While event duration (D) and maximum easterly wind (E_{max}) were listed by Tomikawa (2010), we add the event intensity in terms of accumulated easterlies (I_{acc}). Although at first glance all large-amplitude events are also long in time (like 2006, 2009, and 2013), this does not hold in general. Our results demonstrate how the new-defined event intensity I_{acc} combines available information on amplitude and duration to better evaluate weaker events too.

With reference to the event intensity, we separate strong and weak events with the median as a threshold criterion. This made the classification of the 2008 event difficult because it has exactly the same value as the median. The median values for D, E_{max}, and maximum event intensity (I_{max}) confirmed the 2008 was "at the edge" in terms of classification. However, here we keep the classification of 2008 as a weak event, as in Kishore Kumar et al. (2014).

To evaluate the representativity of our data, we compare D and E_{max} values with the reference data as we did for the event frequency. The ERA/MLS mean values differ from JRA–NCEP (see D and E_{max} in Table 3) with only 11% and 32% significance. We conclude that the event intensity is representative for the climatology. For the comparison with model simulations, we will use the fraction of strong-intensity events (R_{SI} = 0.43) with an error range of 0.23 to 0.63.

With regard to the vortex form (split or displaced) we follow the aspect-ratio decision criterion of Seviour et al. (2013) in a modified time window in comparison to Charlton and Polvani (2007). In addition to the daily vortex form we also give the near-event split-vortex number and frequency (n^*_{SV} and f^*_{SV}). It allows us to distinguish SSW events with many or few split-vortex days. We find most split-vortex days for the 2009 event and gradually fewer for the 2010a and 2013 events. This ranking corresponds to the ranking by intensity and suggests that strong warmings are likely splittings. Exceptions are the 2008 event (strong but displacement) and 2010a event (weak but splitting). However, the rule of thumb holds for mean values. We find for the three splitting events a mean intensity of 144 m s^{-1} day^{-1} and for the four displacement events a mean value of 71 m s^{-1} day^{-1}. Consistent results are found for the mean durations (18 vs 10 days) and maximum easterlies (13 vs 10 m s^{-1}). This is in line with previous analyses of de la Torre et al. (2012) for NCEP–NCAR (1957–2002). From our data we estimate the fraction of split-vortex events as R_{SV} = 0.43. This value differs from the JRA–NCEP data at a level of 15%, which can be considered insignificant. Hence, our estimate of R_{SV} ranging between 0.53 and 0.89 will be taken for the model comparison.

The new parameter completing the classification of SSWs is the daily information on mesospheric couplings. The observed fraction of mesospheric coupling events is $R_{MC} = 0.71$. Although the error is relatively large due to the limited sample size, this number will be included into the comparison with simulations. While R_{MC} is obtained through application of the one-sigma thresholds, the

TABLE 6. Relative model deviations from observations [index (model)/index(observation − 1] for the frequency of major warmings (F_{MV}) and the fraction of strong intensity, split-vortex, and mesospheric coupling events (R_{SI}, R_{SV}, and R_{MC}). Values from Table 2 are used for the observations. The last row contains the root-mean-square deviations (RMS) for each index.

Model	F_{MV}	R_{SI}	R_{SV}	R_{MC}
KMCM	−0.25	−0.67	1.33	−0.20
HAMMONIA	0.33	−0.31	−0.18	−0.18
WACCM	−0.08	−0.56	−0.56	0.31
RMS	0.24	0.54	0.84	0.24

same result is obtained from the analysis of cross-correlations. Comparing Fig. 2b and Table 1, the five anticorrelated events ($r < -0.5$: 2006, 2008, 2009, 2010a, 2013) correspond to the mesospheric coupling class, and the two uncorrelated events ($-0.5 < r < 0.5$: 2007, 2010b) correspond to the major warming class. Hence, the estimate of the fraction of mesospheric coupling events, although based on slightly different methods from the same dataset, can be considered as stable.

c. Comparison with model simulations

The comparison of model simulations with observational data is done with parameters compiled in Table 6. Relative deviations are calculated for each model; this is the difference between observation and simulation normalized to the observed value. It needs to be emphasized that the analysis of these differences is only indicative because of the small number of observed cases.

With regard to the major warming frequency (F_{MW}; Table 6), WACCM appears to simulate it perfectly, whereas in HAMMONIA it is 33% larger and in KMCM 36% lower than in the observations. This finding is not obviously related to specific model features; for example, WACCM includes a QBO but has lower major warming frequency than HAMMONIA without QBO. For KMCM the time-invariant background field could be a reason for the lower stratospheric variability.

An intercomparison of the event intensity (I_{acc}; Table 2) clearly shows that the observed events are on average stronger by a factor of about 2. Consequently, the fraction of strong events (R_{SI}; Table 6) is in the models between 31% and 56% smaller. These discrepancies in both parameters may indicate some insufficiently resolved planetary wave dynamics in the lower and middle atmosphere.

The total-winter frequency of split-vortex days (f^{+}_{SV}; Table 3) is nearly realistic in HAMMONIA and WACCM whereas it is clearly higher in KMCM. However, relative to this quantity, the event-averaged split-vortex frequency ($\bar{f}^{*}_{SV}$; Table 3) is about a factor of 3 larger in the case of the observations. A factor of 3 is also found for HAMMONIA, while it is 4 for KMCM and 8 for WACCM. This supports the statement that vortex splits appear more likely during major warming events. The inspection of the fraction of split-vortex events (R_{SV}, Table 2) comes to similar conclusions. For this parameter, we find that KMCM simulates more while HAMMONIA and WACCM simulate less than observed. In the model comparison (R_{SV}; Table 6) the numbers from HAMMONIA and WACCM are less by 18% and 56%. All events of KMCM appear to be splittings, which means that the relative number of split-vortex events is significantly higher than observed by 133%. A possible reason is the distribution of tropospheric heating sources in this model, which favors planetary-wave-2 structures.

The mesospheric couplings instead seem to be a robust feature. From their daily statistics we find nearly identical total-winter frequencies (f^{+}_{MC}; Table 3). The relative event-averaged frequencies ($\bar{f}^{*}_{MC}/f^{+}_{MC}$) suggest, with numbers between 2 and 4, that mesospheric couplings are more likely during major warmings. Using the event statistics we find from comparing the fraction of mesospheric coupling events (R_{MC}; Table 6) that all models are similar to the observations: values are in KMCM 20% lower, in HAMMONIA 18% lower, and in WACCM 31% higher. The range of simulated values (0.57–0.94) fits the error range of the observations (0.53–0.89; see R_{MC} in Table 2). Although the differences are statistically insignificant they allow for a qualitative interpretation. The dynamic coupling between stratospheric warmings and mesospheric coolings is mainly realized by GWs, as outlined by Zülicke and Becker (2013). These waves are resolved in KMCM, while they were parameterized in the other two models. However, this model feature alone does not explain the differences in this comparison.

Do simulations show the hypothesized link between mesospheric couplings and event intensity or vortex form as diagnosed from 10-hPa data? In review of Table 4 (columns $r_{MC–SI}$ and $r_{MC–SV}$) we find only weak correlations with explained variances below 30%. On the contrary, using data between 10- and 0.1-hPa levels, Fig. 4 shows that mesospheric couplings are associated with deep easterlies for both observations and simulations. Corresponding correlations of mesospheric couplings with the model-derived GW phase speed (Table 4, column $r_{MC–GW}$) also document a relatively homogeneous behavior with explained variances above 40%.

d. Identification of the relevant process

For the further interpretation of the statistical results a conceptual model is used. It predicts the thermal response of the mesosphere to dominating zonal-mean easterly winds in the stratosphere as result of a

GW-induced dynamic cooling. The model allows us to study the influence of the form of the stratospheric vortex on the zonal-mean GW forcing as was shown qualitatively by Dunkerton and Butchard (1984). The relative simplicity of the conceptual model allows for the derivation of a typical relation between stratospheric wind and mesospheric GW phase speed (such as shown in Fig. 5), which summarizes the essential filtering effects. As long as this relation is linear, the dominance of easterlies in a wind profile implies a positive GW phase speed respectively a dynamic cooling.

Using the ERA winds in the conceptual model, an influence of strong major warmings on mesospheric couplings is confirmed. Further, we highlight the influence of the vertical structure of the zonal-mean zonal wind. The deeper the zonal-mean easterlies, the more likely a mesospheric coupling; in other words, the wind has to provide a ''gravity wave guide.'' This deep/coupled hypothesis (based on three wind levels) is shown to explain more variability in the daily mesospheric couplings than the strong/coupled or the split/coupled hypothesis (based on one wind level).

The time series indicate that the timing of deep easterlies with respect to the major warming central date is quite variable and deserves further investigation. The assumption of a finite and constant GW launch spectrum for the conceptual model leads to reasonable results in application to the four datasets in this study. However, it is very likely that a wider spectrum and additional GW sources may appear associated with strong planetary wave activity including local storms and jet/front systems (Mirzaei et al. 2014). Although such effects are not obvious in the present analysis, this issue is worth further consideration. Additionally, the observational data do not allow for an identification of the effects of planetary-wave amplitude and wavenumber with the conceptual GW propagation model. While evidence was reported for preferred barotropic structure of split vortices (Matthewman et al. 2009) and associated stratopause responses (Vignon and Mitchell 2015), we could not further support the split/coupled hypothesis because the zonal-mean winds dominated the zonal-mean GW behavior in the analyzed observations. More events with wider spread polar vortex structures are needed to obtain more refined statistics of the GW effects in the mesosphere.

5. Summary and conclusions

The stratosphere–mesosphere coupling is studied with a new diagnostic method, which is used to classify major sudden stratospheric warmings (SSWs), to quantify their statistical properties, and to identify the process relevant for the coupling. To obtain the most complete understanding of the stratosphere–mesosphere problem possible, we use a range of different observations and simulations.

In addition to the commonly used stratospheric characteristics of SSW events, we suggest a new objective method to diagnose those extending vertically into the mesosphere. For that purpose the 60°–90°N polar cap temperature is analyzed. If at the same day both a warm middle stratosphere at 10 hPa and a cold upper mesosphere at 0.01 hPa are found, it is termed a ''mesospheric coupling'' (MC). In general, this method is relatively simple, using a one-sigma criterion to detect anomalies. Because of its simplicity the proposed diagnostics could be further extended upward to find upper-atmosphere SSW-related anomalies on a daily basis.

Application of the mesospheric coupling diagnostics to daily Aura-MLS data from 2004 to 2015 reveals a total frequency of 7% mesospheric coupling days in winter. This shows that anomalous stratosphere–mesosphere coupling is a quite frequent phenomenon. During major sudden stratospheric warmings the mesospheric coupling frequency is on average 22%, indicating an intensified vertical coupling. It is different from event to event, which allows for a classification of major warmings. Of the diagnosed seven major warming events in observations, five were found to be coupled to the mesosphere (2006, 2008, 2009, 2010, and 2013). This new information is added to commonly used documentations of major warmings up to and including the 2013 event (Table 1). It covers information on the event intensity (Tomikawa 2010) and the vortex form (Cohen and Jones 2011; Hitchcock et al. 2013; Seviour et al. 2013; Barriopedro and Calvo 2014). From these parameters we find that the 2013 major warming event is the third most intense after 2009 and 2006. The mesospheric coupling event classification completes the information derived from the diagnosis of elevated stratopause events using a stratopause-tracking algorithm, polar-night jet oscillations (PJOs), principal component analysis, and anomalous strong descent events of passive tracers. The three strongest events all show mesospheric structures in these four classifications while the situation is less distinct for the weaker events. Hence, detection of mesospheric coupling during the initial and peak phase of a strong SSW is found to be linked to the elevated stratopause, PJO, and strong descent features during its recovery phase.

In comparison with the observed fraction of mesospheric coupling events (5 of 7, 71%), the three simulations perform adequately with fractions between 57% and 94% (R_{MC}; Table 2). The relatively small root-mean-square (RMS) deviation of simulations from observations of 24% (R_{MC}; Table 6) is interpreted as a hint as to the overall robustness of simulations that are not

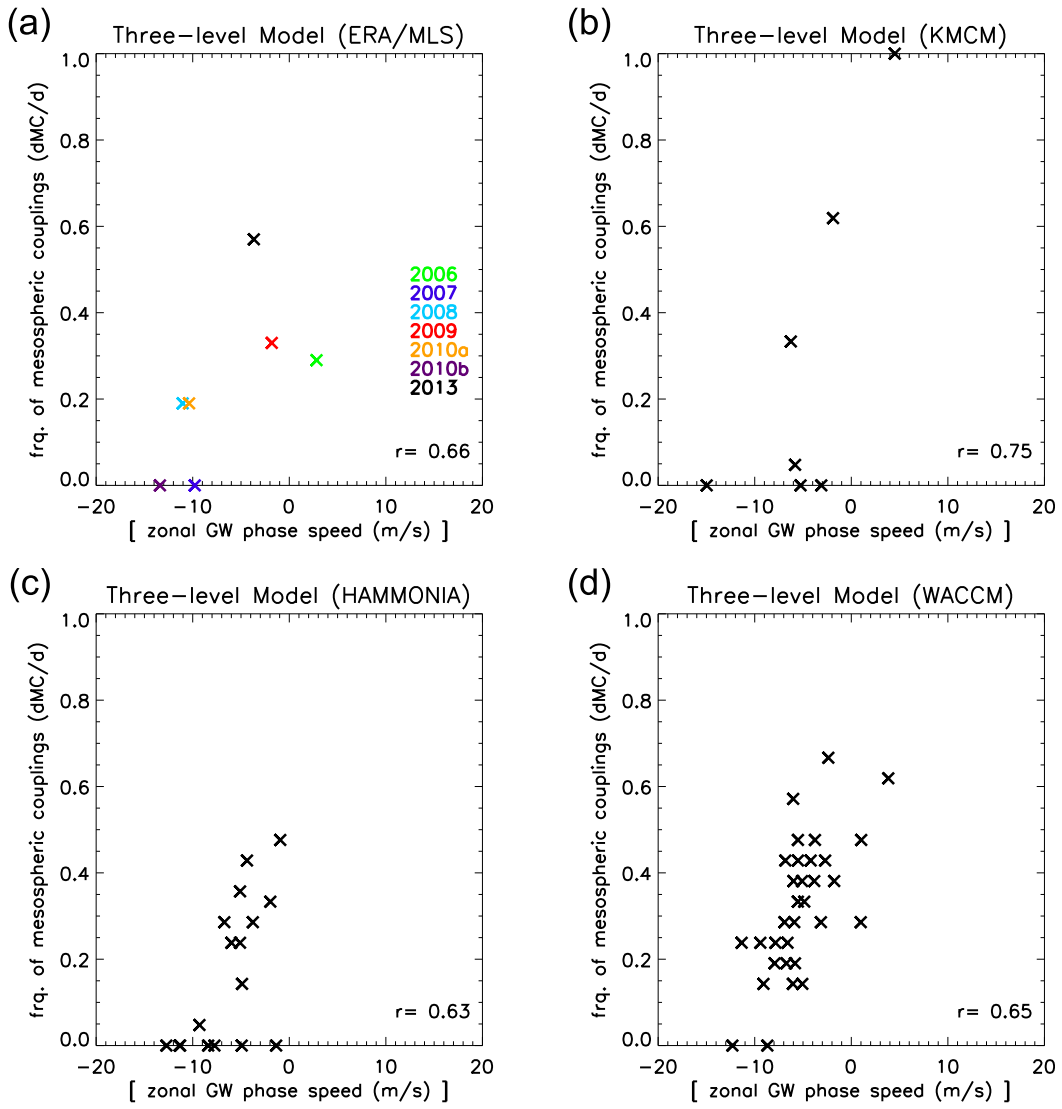

FIG. 8. Scatterplots of the near-event frequency of mesospheric couplings (f^*_{MC}) vs the model-derived zonal-mean zonal GW phase speed ($[c^*_{\mathrm{GW}}]$) for (a) ERA/MLS, (b) KMCM, (c) HAMMONIA, and (d) WACCM. The correlation coefficient is given in the lower-right corner.

sensitive to the details of gravity wave treatment in the different models. Once a stratospheric warming occurs, the gravity waves communicate this information quickly into the mesosphere. The frequency of major warmings (F_{MW}; Table 6) shows an RMS deviation over all models of 28%. This is the result of considerable model improvements over the last decades. The fraction of strong intensity events is too low for all models with an RMS of 54% (R_{SI}; Table 6). Even larger RMS deviations of 84% are found for the fraction of split-vortex events (R_{SV}; Table 6). We take the relative high RMS deviations for the SSW intensity and split vortices as an indication for deficiencies in the simulation of stratospheric planetary waves.

Searching for causal relations, hypotheses relating the frequency of mesospheric couplings during major warmings to the event intensity and the vortex form have been tested: 1) the stronger the 10-hPa easterlies are, or 2) the more frequent the vortex is split at this level, the more likely is a coupling to the mesosphere. However, the explained variances (see Table 4) of below 30% allow only for an interpretation as a weak indication for such linear relations. More evidence is obtained from a conceptual model for the influence of the zonal wind profile on the gravity wave propagation (Fig. 4). In particular, the depth of zonal-mean easterlies between 10 and 0.1 hPa was found to be relevant and to explain more than 40% of the variance (Fig. 8). This means the stratospheric wind

needs to provide a gravity-wave guide for a vertical coupling to occur. These statistical tests indicate that indices constructed from single stratospheric levels like 10 hPa may give a hint as to the vertical coupling with the mesosphere but the vertical structure of the whole stratosphere has to be taken into account for a more adequate picture. The instance when all four datasets show similar levels of correlation between mesospheric coupling and conceptual model indicates a near-realistic simulation of the underlying gravity wave propagation process.

Finally, it is reiterated that the presented numbers are associated with several shortcomings and care is recommended for their interpretation. The 11 years of observations used in our study provide stratospheric indices similar to those obtained in earlier studies of longer time series but, of course, the frequency of mesospheric coupling may not be climatologically representative. Additionally, both observations and simulations contain considerable internal variability, which makes it difficult to identify simple causal relations. Therefore, further theoretical and statistical investigation of stratosphere–mesosphere coupling with a wider database seems advisable, although currently no such observational dataset with sufficient coverage of the mesosphere exists. However, the presented intercomparison of observations with simulations using an objective diagnostics provides a framework to benchmark the data and to identify the relevant dynamical mechanisms.

Acknowledgments. We thank Peter Hitchcock, Andy Miller, Diane Pendlebury, Peter Hoffmann, and the members of ISSI Teams 217 and 320, sponsored by the International Space Science Institute (Bern, Switzerland), for helpful discussions. The constructive comments of three anonymous referees are highly appreciated. We acknowledge the German Weather Service (DWD) and the ECMWF, the Jet Propulsion Laboratory, and NASA for data provision and user support. Simulation data are available on request from EB (KMCM), HS (HAMMONIA), and HLL (WACCM). The research of LTR was funded by the Spanish Ministry of Economy and Competitiveness through the project CGL2011-2486. The studies of VM were funded by the Leibniz Gemeinschaft through the SAW project LOCHMES (Long-Term Changes in the Mesosphere, SAW-2011-IAP-1). CZ and HS acknowledge support from the Deutsche Forschungsgemeinschaft (DFG) for the research unit MS-GWaves (Multi-Scale dynamics of Gravity Waves) through Grants ZU 120/2-1 [project SI (Spontaneous Imbalance)] and SCHM 2158/5-1 [project GWING (Gravity Waves in Global Context)].

APPENDIX A

Definitions

Definitions (units) used in the diagnostics are given in alphabetical order:

$$D = \text{event duration (number of days with easterly wind) (days)}, \tag{A1}$$

$$\overline{D} = \sum_{i_{\mathrm{MW}}=1}^{N_{\mathrm{MW}}} \frac{D(i_{\mathrm{MW}})}{N_{\mathrm{MW}}} = \text{event-averaged duration (number of days with easterly wind) (days)}, \tag{A2}$$

$$E = \text{daily-mean easterly wind (m s}^{-1}\text{)}, \tag{A3}$$

$$E_{\max} = \text{maximum easterly wind during event (m s}^{-1}\text{)}, \tag{A4}$$

$$\overline{E}_{\max} = \sum_{i_{\mathrm{MW}}=1}^{N_{\mathrm{MW}}} \frac{E_{\max}(i_{\mathrm{MW}})}{N_{\mathrm{MW}}} = \text{event-averaged maximum easterly wind (m s}^{-1}\text{)}, \tag{A5}$$

$$F_{\mathrm{MW}} = \frac{N_{\mathrm{MW}}}{T} = \text{frequency of major warming events (\#MW yr}^{-1}\text{)}, \tag{A6}$$

$$f_{\mathrm{MC}} = \frac{n_{\mathrm{MC}}}{T} = \text{total frequency of mesospheric-coupling days (dMC day}^{-1}\text{)}, \tag{A7}$$

$$f_{\mathrm{MC}}^{+} = \frac{n_{\mathrm{MC}}^{+}}{T_{+}} = \text{total-winter frequency of mesospheric-coupling days (dMC day}^{-1}\text{)}, \tag{A8}$$

$$f^*_{\mathrm{MC}} = \frac{n^*_{\mathrm{MC}}}{T_*} = \text{near-event frequency of mesospheric-coupling days (dMC day}^{-1}\text{)}, \tag{A9}$$

$$\overline{f}^*_{\mathrm{MC}} = \sum_{i_{\mathrm{MW}}=1}^{N_{\mathrm{MW}}} \frac{f^*_{\mathrm{MC}}(i_{\mathrm{MW}})}{N_{\mathrm{MW}}} = \text{event-averaged frequency of mesospheric-coupling days (dMC day}^{-1}\text{)}, \tag{A10}$$

$$f_{\mathrm{SV}} = \frac{n_{\mathrm{SV}}}{T} = \text{total frequency of split-vortex days (dSV day}^{-1}\text{)}, \tag{A11}$$

$$f^+_{\mathrm{SV}} = \frac{n^+_{\mathrm{SV}}}{T_+} = \text{total-winter frequency of split-vortex days (dSV day}^{-1}\text{)}, \tag{A12}$$

$$f^*_{\mathrm{SV}} = \frac{n^*_{\mathrm{SV}}}{T_*} = \text{near-event frequency of split-vortex days (dSV day}^{-1}\text{)}, \tag{A13}$$

$$\overline{f}^*_{\mathrm{SV}} = \sum_{i_{\mathrm{MW}}=1}^{N_{\mathrm{MW}}} \frac{f^*_{\mathrm{SV}}(i_{\mathrm{MW}})}{N_{\mathrm{MW}}} = \text{event-averaged frequency of split-vortex days (dSV day}^{-1}\text{)}, \tag{A14}$$

$$I_{\mathrm{acc}} = \sum_{t=1\mathrm{day}}^{T} (\mathrm{SWM}_t = \mathrm{MW})E = \text{event intensity based on accumulated easterlies (m s}^{-1}\text{ day)}, \tag{A15}$$

$$\overline{I}_{\mathrm{acc}} = \sum_{i_{\mathrm{MW}}=1}^{N_{\mathrm{MW}}} \frac{I_{\mathrm{acc}}(i_{\mathrm{MW}})}{N_{\mathrm{MW}}} = \text{event-averaged intensity (m s}^{-1}\text{ day)}, \tag{A16}$$

$$I_{\mathrm{max}} = DE_{\mathrm{max}} = \text{maximum event intensity based on the maximum easterly (m s}^{-1}\text{ day)}, \tag{A17}$$

$$N_{\mathrm{MC}} = \sum_{i_{\mathrm{MW}}=1}^{N_{\mathrm{MW}}} [f^*_{\mathrm{MC}}(i_{\mathrm{MW}}) > 0] = \text{number of mesospheric-coupling events (\#MC)}, \tag{A18}$$

$$N_{\mathrm{MW}} = \text{number of major warming events (\#MW)}, \tag{A19}$$

$$N_{\mathrm{SI}} = \sum_{i_{\mathrm{MW}}=1}^{N_{\mathrm{MW}}} [I_{\mathrm{acc}}(i_{\mathrm{MW}}) > 50\,\mathrm{m\,s^{-1}\,day}] = \text{number of strong-intensity events (\#SI)}, \tag{A20}$$

$$N_{\mathrm{SV}} = \sum_{i_{\mathrm{MW}}=1}^{N_{\mathrm{MW}}} [f^*_{\mathrm{SV}}(i_{\mathrm{MW}}) > 0] = \text{number of split-vortex events (\#SV)}, \tag{A21}$$

$$n_{\mathrm{MC}} = \sum_{t=1\mathrm{day}}^{T} (\mathrm{SWX}_t = \mathrm{MC}) = \text{total number of mesospheric-coupling days (dMC)}, \tag{A22}$$

$$n^+_{\mathrm{MC}} = \sum_{t_+=1\mathrm{day}}^{T_+} (\mathrm{SWX}_t = \mathrm{MC}) = \text{total-winter number of mesospheric-coupling days (dMC)}, \tag{A23}$$

$$n^*_{\mathrm{MC}} = \sum_{t=t_{\mathrm{cen}}-10\mathrm{day}}^{t_{\mathrm{cen}}+10\mathrm{day}} (\mathrm{SWX}_t = \mathrm{MC}) = \text{near-event number of mesospheric-coupling days (dMC)}, \tag{A24}$$

$$\hat{n}^*_{\mathrm{MC}} = \sum_{i_{\mathrm{MW}}=1}^{N_{\mathrm{MW}}} n^*_{\mathrm{MC}}(i_{\mathrm{MW}}) = \text{event-accumulated number of mesospheric-coupling days (dMC)}, \tag{A25}$$

$$n_{\mathrm{SV}} = \sum_{t=1\mathrm{day}}^{T} (\mathrm{SWE}_t = \mathrm{SV}) = \text{total number of split-vortex days (dSV)}, \tag{A26}$$

$$n^+_{\mathrm{SV}} = \sum_{t_+=1\mathrm{day}}^{T_+} (\mathrm{SWE}_t = \mathrm{SV}) = \text{total-winter number of split-vortex days (dSV)}, \tag{A27}$$

$$n^*_{\mathrm{SV}} = \sum_{t=t_{\mathrm{cen}}-10\mathrm{day}}^{t_{\mathrm{cen}}+10\mathrm{day}} (\mathrm{SWE}_t = \mathrm{SV}) = \text{event number of split-vortex days (dSV)}, \tag{A28}$$

$$\hat{n}^{*}_{\mathrm{SV}} = \sum_{i_{\mathrm{MW}}=1}^{N_{\mathrm{MW}}} n^{*}_{\mathrm{SV}}(i_{\mathrm{MW}}) = \text{event-accumulated number of split-vortex days (dSV)}, \tag{A29}$$

$$R_{\mathrm{MC}} = \frac{N_{\mathrm{MC}}}{N_{\mathrm{MW}}} = \text{fraction of mesospheric-coupling events (\#MC/\#MW)}, \tag{A30}$$

$$R_{\mathrm{SI}} = \frac{N_{\mathrm{SI}}}{N_{\mathrm{MW}}} = \text{fraction of strong-intensity events (\#SI/\#MW)}, \tag{A31}$$

$$R_{\mathrm{SV}} = \frac{N_{\mathrm{SV}}}{N_{\mathrm{MW}}} = \text{fraction of split-vortex events (\#SV/\#MW)}, \tag{A32}$$

$$T = \text{total length of time series (day)}, \tag{A33}$$

$$T_{+} = \text{total length of winters (from 1 November to 31 March) (days)}, \tag{A34}$$

$$T_{*} = 21\ \text{day} = \text{length of time window around the central day of major warming, and} \tag{A35}$$

$$t_{\mathrm{cen}} = \text{central date (the first day with easterly wind)}. \tag{A36}$$

APPENDIX B

Geometrical Moments

The elliptic vortex diagnostics estimates the geometrical properties of the polar vortex following Mitchell et al. (2011). For a given field q, the vortex edge q_{edge} is set with a weighting function to be used with the zonal-mean values $q_z(\phi) = \langle q(\lambda, \phi)\rangle_{\lambda}$ in

$$q_{\mathrm{edge}} = \frac{\langle w_z(\phi)\, q_z(\phi)\rangle\phi}{\langle w_z(\phi)\rangle\phi}. \tag{B1}$$

In this study, we use the adjusted gradient according to

$$w_z = [q_{z,+} > \max(q_{z,+})/3], \tag{B2}$$

where the meridional gradient of the zonal-mean value $q_{z,\phi} = (\partial q_z/\partial\phi) \times (|\phi| > 45°)\mathrm{N}$ and the positive-only gradient $q_{z,+} = q_{z,\phi} \times (q_{z,\phi} > 0)$ were used, each in the region poleward of 45°N.

This threshold value defines the shape of the vortex with a conventional area of

$$A = \int dx \int dy (q > q_{\mathrm{edge}}). \tag{B3}$$

For the following method, the local weights

$$\hat{q}(x, y) = (q - q_{\mathrm{edge}}) \times (q > q_{\mathrm{edge}}) \tag{B4}$$

are used. Absolute moments defined as

$$M_{kl} = \int dx \int dy\, \hat{q} x^k y^l \tag{B5}$$

are used for the determination of the centroid $(\overline{x}, \overline{y})$ and the equivalent or objective area A_{obj}:

$$(\overline{x}, \overline{y}) = \left(\frac{M_{10}}{M_{00}}, \frac{M_{01}}{M_{00}}\right), \quad \text{and} \tag{B6}$$

$$A_{\mathrm{obj}} = \frac{M_{00}}{q_{\mathrm{edge}}}.$$

With the relative moments

$$J_{kl} = \int dx \int dy\, \hat{q}(x - \overline{x})^k (y - \overline{y})^l \tag{B7}$$

the angle of the major axis θ, the aspect ratio a, and the kurtosis κ_4 are found:

$$\theta = \frac{1}{2}\arctan\left(\frac{2J_{11}}{J_{20} - J_{02}}\right), \tag{B8}$$

$$a = \left|\frac{(J_{20} + J_{02}) + [4J_{11}^2 + (J_{20} - J_{02})^2]^{1/2}}{(J_{20} + J_{02}) - [4J_{11}^2 + (J_{20} - J_{02})^2]^{1/2}}\right|^{1/2}, \quad \text{and}$$

$$\kappa_4 = J_{00}\frac{J_{40} + 2J_{22} + J_{04}}{(J_{02} + J_{20})^2} - \frac{2}{3}\frac{3a^4 + 2a^2 + 3}{(1 + a^2)^2}.$$

APPENDIX C

Averaging Procedure

The mesospheric coupling diagnostics requires daily mean values and standard deviations. Given is the temperature time series $T(d, y)$ depending on time

through the day number (d = 1–365) and the year number (y = 1–11). The seasonal (intra-annual) mean is formed with a running 91-day Lanczos filter, expressed with the weighting function w_{91d} as

$$T_{91\mathrm{d}}(d,y) = \sum_{d'=-45}^{45} w_{91\mathrm{d}}(d')T(d+d',y), \quad \text{and} \tag{C1}$$

$$s^2_{91\mathrm{d}}(d,y) = \sum_{d'=-45}^{45} w_{91\mathrm{d}}(d')[T(d+d',y) - T_{91\mathrm{d}}(d+d',y)]^2.$$

The year-to-year (interannual) mean is formed from averaging each day-of-the-year over the 11 years, that is

$$T_{11\mathrm{y}}(d) = \frac{1}{11}\sum_{y=1}^{11} T(d,y), \quad \text{and} \tag{C2}$$

$$s^2_{11\mathrm{y}}(d) = \frac{1}{11}\sum_{y=1}^{11} [T(d,y) - T_{11\mathrm{y}}(d)]^2.$$

Together, the mean and standard deviation used for the one-sigma criterion are

$$T_{91\mathrm{d},11\mathrm{y}}(d) = \frac{1}{11}\sum_{y=1}^{11}\sum_{d'=-45}^{45} w_{91\mathrm{d}}\, T(d+d',y), \tag{C3}$$

$$s^2_{91\mathrm{d},11\mathrm{y}}(d) = \frac{1}{11}\sum_{y=1}^{11}\sum_{d'=-45}^{45} w_{91\mathrm{d}}(d')[T(d+d',y) - T_{91\mathrm{d},11\mathrm{y}}(d)]^2,$$

$$= \frac{1}{11}\sum_{y=1}^{11} s^2_{91\mathrm{d}}(d,y) + \frac{1}{11}\sum_{y=1}^{11} [T_{91\mathrm{d}}(d,y) - T_{91\mathrm{d},11\mathrm{y}}(d)]^2.$$

The variance is composed of the interannual mean of seasonal variance and the interannual variance of the seasonal means.

APPENDIX D

Gravity Wave Propagation Model

The vertical propagation of GW packets is treated in column approximation; that is, the wind is assumed to be much slower than the waves and its horizontal variations are much larger. A broadband zonal GW phase speed spectrum

$$f_0(c') = \begin{cases} -1: & -c_0 < c' < \\ +1: & 0 < c' < c_0 \\ 0: & \text{else} \end{cases} \tag{D1}$$

is launched in the lower stratosphere (at 10-km height) that includes sample phase speeds (c') between $-c_0$ and $+c_0$ with c_0 fixed to 15 m s^{-1}. This choice is based on typical values for the midlatitude inertia–gravity waves (Zülicke and Peters 2008): 350-km horizontal wavelength and 6-h intrinsic period. In the middle mesosphere (at 80-km height) the averaged phase speed (c_{GW}) is calculated from the integral over the mesospheric distribution of sample phase speeds f, that is

$$c_{\mathrm{GW}} = \int dc'\, f(c'). \tag{D2}$$

The filter effect of the stratospheric zonal wind, which is supposed to be zero at the ground, is examined at each longitude: Positive phase speeds between zero and the maximum wind of the local profile

$$u_+ = \max(0,u) \tag{D3}$$

are filtered out, leading to a contribution of

$$c_+ = \begin{cases} c_0: & u_+ < 0 \\ (c_0 - u_+): & 0 < u_+ < c_0 \\ 0: & c_0 < u_+ \end{cases}. \tag{D4}$$

Correspondingly, all negative phase speeds between zero and the minimum wind

$$u_- = \min(0,u) \tag{D5}$$

are filtered, leaving a contribution of

$$c_- = \begin{cases} 0: & u_- < -c_0 \\ -(c_0 + u_-): & -c_0 < u_- < 0 \\ -c_0: & 0 < u_- \end{cases}. \tag{D6}$$

The local phase speed at 80-km height is then found from the sum of (D4) and (D6) as

$$c_{\mathrm{GW}} = c_+ + c_-. \tag{D7}$$

The model equations are solved numerically for height-dependent and longitude-dependent zonal wind fields.

Analytical solutions can be given if the minimum and maximum values of the wind profile are known. For a moderate minimal wind ($-c_0 < u_{\min} < 0$) and an arbitrary maximal wind ($u_{\max}$) we find a phase speed of

$$c_{\mathrm{GW}}(u_{\min},u_{\max}) = \begin{cases} -u_{\min}: & -c_0 < u_{\min} < u_{\max} < 0 \\ -u_{\min} - u_{\max}: & -c_0 < u_{\min} < 0 < u_{\max} < c_0 \\ -u_{\min} - c_0: & -c_0 < u_{\min} < 0 < c_0 < u_{\max} \end{cases}. \tag{D8}$$

This is the dashed line in Fig. 5; the phase speed is zero for

$$u_{\max} = -u_{\min}. \tag{D9}$$

APPENDIX E

Gravity Wave Forcing in the Mesosphere

The forcing of the mesospheric circulation by GWs is considered in order to derive a relation between temperature anomalies and the GW phase speed. According to Holton (1982) the zonal-mean residual circulation is driven by the zonal GW pseudomomentum flux (GWF) divergence

$$f v_* = \frac{\partial \mathrm{GWF}}{\partial z}. \tag{E1}$$

The induced residual meridional circulation v_* enforces a certain vertical motion w_* through the continuity equation

$$w_* = -\int dz \frac{\partial v_*}{\partial y}. \tag{E2}$$

From the thermodynamic equation, which is modeled as a radiative relaxation to an equilibrium temperature T_e,

$$\frac{\partial \theta_0}{\partial z} w_* = \gamma (T_e - T) \tag{E3}$$

the dynamically forced temperature is found to be

$$T = T_e + \int dz \frac{\partial \theta_0}{\partial z} \frac{1}{\gamma f} \frac{\partial^2 \mathrm{GWF}}{\partial y \partial z}. \tag{E4}$$

To estimate the mesospheric polar-cap temperature, we integrate vertically from the stratopause (at about 50 km) to the mesopause (at about 80 km) and assume that all GWF is dissipated over this vertical scale ($L_z = 30$ km). Further, the relevant meridional GWF gradient is assumed to be placed between 60° and 90°N, i.e., over a meridional scale of $L_y = 3300$ km. An average over these scales leads to the mesospheric polar-cap temperature anomaly estimate of

$$T'_{\mathrm{PC}} = T_{\mathrm{PC}} - T_e \approx -\frac{\partial \theta_0}{\partial z} \frac{\mathrm{GWF}}{\gamma f L_y} \doteqdot -C_F \, \mathrm{GWF}, \tag{E5}$$

which appears to be related to the negative stratopause GWF.

The next step is the consideration of the zonal GW phase speed. For this purpose the pseudomomentum flux definition

$$\mathrm{GWF} = k_x \, c_{g,z} \frac{e}{\hat{\omega}} \tag{E6}$$

is used, which includes the zonal wavenumber k_x, the energy e, the intrinsic frequency

$$\hat{\omega} = -N \frac{|k_x|}{k_z} = k_x (c_{p,x} - u) > 0, \tag{E7}$$

and the vertical group velocity

$$c_{g,z} = \frac{\partial \hat{\omega}}{\partial k_z} = N \frac{|k_x|}{k_z^2} > 0, \tag{E8}$$

which are readily specified for midfrequency upward-propagating GWs ($k_z < 0$) in column approximation. Hence, the GWF is found to be proportional to the intrinsic phase speed

$$\mathrm{GWF} = -\frac{k_x}{k_z} e = (c_{p,x} - u) \frac{|k_x|}{N} e = C_c (c_{p,x} - u). \tag{E9}$$

These approximations also give reasonable estimates: As a check value we adopt a mesospheric GW drag of $50\,\mathrm{m\,s^{-1}\,day^{-1}}$, which corresponds to a stratopause-level GWF of $17\,\mathrm{m^2\,s^{-2}}$. With a Coriolis parameter $f = 1.4 \times 10^{-4}\,\mathrm{rad\,s^{-1}}$, a Brunt–Väisälä frequency $N = 2 \times 10^{-2}\,\mathrm{rad\,s^{-1}}$, a temperature gradient $\partial\theta_0/\partial z = 2\,\mathrm{K\,km^{-1}}$, and a thermal relaxation coefficient of $\gamma = (5\ \mathrm{days})^{-1}$ we find from Eq. (E5) a momentum-flux factor $C_F = 1.9\,\mathrm{K\,s^2\,m^{-2}}$ and a related temperature anomaly of 32 K. The phase-speed factor C_c is calibrated with Eq. (E9) using the vertical wavenumber of $k_z = 2\pi(5\,\mathrm{km})^{-1}$ to be $\mathrm{GWF} k_z N^{-1} = 1.1\,\mathrm{m\,s^{-1}}$ and used to estimate a GW phase speed of $16\,\mathrm{m\,s^{-1}}$. These are the considered orders of magnitude.

In the statistical analysis we use the relation obtained from Eqs. (E5) and (E9)

$$T'_{\mathrm{PC}} \approx -C_F C_c c_p \tag{E10}$$

to associate a positive zonal GW phase speed to dynamic cooling. We provide the mean wind in the upper mesosphere is weaker than the phase speed, which is consistent with the considered GW spectrum.

REFERENCES

Andrews, D. G., J. R. Holton, and C. B. Leovy, 1987: *Middle Atmosphere Dynamics*. International Geophysics Series, Vol. 40, Academic Press, 489 pp.

Bailey, S. M., and Coauthors, 2014: A multi tracer analysis of thermosphere to stratosphere descent triggered by the 2013 stratospheric sudden warming. *Geophys. Res. Lett.*, **41**, 5216–5222, https://doi.org/10.1002/2014GL059860.

Baldwin, M. P., and T. J. Dunkerton, 1999: Propagation of the Arctic Oscillation from the stratosphere to the troposphere. *J. Geophys. Res.*, **104**, 30 937–30 946, https://doi.org/10.1029/1999JD900445.

Barriopedro, D., and N. Calvo, 2014: On the relationship between ENSO, stratospheric sudden warmings, and blocking. *J. Climate*, **27**, 4704–4720, https://doi.org/10.1175/JCLI-D-13-00770.1.

Becker, E., 2009: Sensitivity of the upper mesosphere to the Lorenz energy cycle of the troposphere. *J. Atmos. Sci.*, **66**, 647–666, https://doi.org/10.1175/2008JAS2735.1.

Butler, A. H., D. J. Seidel, S. C. Hardiman, N. Butchart, T. Birner, and A. Match, 2015: Defining sudden stratospheric warmings. *Bull. Amer. Meteor. Soc.*, **96**, 1913–1928, https://doi.org/10.1175/BAMS-D-13-00173.1.

Chandran, A., R. L. Collins, and V. L. Harvey, 2014: Stratosphere–mesosphere coupling during stratospheric sudden warming events. *Adv. Space Res.*, **53**, 1265–1289, https://doi.org/10.1016/j.asr.2014.02.005.

Charlton, A. J., and L. M. Polvani, 2007: A new look at stratospheric sudden warmings: Part I: Climatology and modeling benchmarks. *J. Climate*, **20**, 449–469, https://doi.org/10.1175/JCLI3996.1.

Charlton-Perez, A. J., and L. M. Polvani, 2011: Corrigendum. *J. Climate*, **24**, 5951, https://doi.org/10.1175/JCLI-D-11-00348.1.

Chau, J. L., B. G. Fejer, and L. P. Goncharenko, 2009: Quiet variability of equatorial E × B drifts during a sudden stratospheric warming event. *Geophys. Res. Lett.*, **36**, L05101, https://doi.org/10.1029/2008GL036785.

Cohen, J., and J. Jones, 2011: Tropospheric precursors and stratospheric warmings. *J. Climate*, **24**, 6562–6572, https://doi.org/10.1175/2011JCLI4160.1.

Dee, D. P., and Coauthors, 2011: The ERA-Interim reanalysis: Configuration and performance of the data assimilation system. *Quart. J. Roy. Meteor. Soc.*, **137**, 553–597, https://doi.org/10.1002/qj.828.

de la Torre, L., R. R. Garcia, D. Barriopedro, and A. Chandran, 2012: Climatology and characteristics of stratospheric sudden warmings in the Whole Atmosphere Community Climate Model. *J. Geophys. Res.*, **117**, D04110, https://doi.org/10.1029/2011JD016840.

Dunkerton, T. J., and N. Butchard, 1984: Propagation and selective transmission of internal gravity waves in a sudden warming. *J. Atmos. Sci.*, **41**, 1443–1460, https://doi.org/10.1175/1520-0469(1984)041<1443:PASTOI>2.0.CO;2.

ECMWF, 2016: IFS Documentation, Cy41r2: Operational implementation 8 March 2016. ECMWF, https://www.ecmwf.int/en/forecasts/documentation-and-support/changes-ecmwf-model/ifs-documentation.

Fuller-Rowell, T., F. Wu, R. A. Akmaev, T.-W. Fang, and E. Araujo-Pradere, 2010: A Whole Atmosphere Model simulation of the impact of a sudden stratospheric warming on the thermosphere dynamics and electrodynamics. *J. Geophys. Res.*, **115**, A00G08, https://doi.org/10.1029/2010JA015524.

Funke, B., M. López-Puertas, D. Bermejo-Pantaleón, M. García-Comas, G. Stiller, T. von Clarmann, M. Kiefer, and A. Linden, 2010: Evidence for dynamical coupling from the lower atmosphere to the thermosphere during a major stratospheric warming event. *Geophys. Res. Lett.*, **37**, L13803, https://doi.org/10.1029/2010GL043619.

Gerber, E. P., and Coauthors, 2010: Stratosphere–troposphere coupling and annular mode variability in chemistry–climate models. *J. Geophys. Res.*, **115**, D00M06, https://doi.org/10.1029/2009JD013770.

Goncharenko, L. P., and S.-R. Zhang, 2008: Ionospheric signatures of sudden stratospheric warming: Ion temperature at middle latitude. *Geophys. Res. Lett.*, **35**, L21103, https://doi.org/10.1029/2008GL035684.

Hines, C. O., 1997: Doppler-spread parameterization of gravity-wave momentum deposition in the middle atmosphere. Part 2: Broad and quasi-monochromatic spectra, and implementation. *J. Atmos. Sol.-Terr. Phys.*, **59**, 387–400, https://doi.org/10.1016/S1364-6826(96)00080-6.

Hitchcock, P., and T. G. Shepherd, 2013: Zonal-mean dynamics of extended recoveries from stratospheric sudden warmings. *J. Atmos. Sci.*, **70**, 688–707, https://doi.org/10.1175/JAS-D-12-0111.1.

——, ——, and G. L. Manney, 2013: Statistical characterization of arctic polar-night jet oscillation events. *J. Climate*, **26**, 2096–2116, https://doi.org/10.1175/JCLI-D-12-00202.1.

Holton, J. R., 1982: The role of gravity wave induced drag and diffusion in the momentum budget of the mesosphere. *J. Atmos. Sci.*, **39**, 791–799, https://doi.org/10.1175/1520-0469(1982)039<0791:TROGWI>2.0.CO;2.

Karlsson, B., C. McLandress, and T. G. Shepherd, 2009: Inter-hemispheric mesospheric coupling in a comprehensive middle atmosphere model. *J. Atmos. Sol.-Terr. Phys.*, **71**, 518–530, https://doi.org/10.1016/j.jastp.2008.08.006.

Kishore Kumar, G., and Coauthors, 2014: Mesosphere and lower thermosphere zonal wind over low latitudes: Relation to local stratospheric zonal winds and global circulation anomalies. *J. Geophys. Res. Atmos.*, **119**, 5913–5927, https://doi.org/10.1002/2014JD021610.

Körnich, H., G. Schmitz, and E. Becker, 2006: The role of stationary waves in the maintenance of the northern annular mode as deduced from model experiments. *J. Atmos. Sci.*, **63**, 2931–2947, https://doi.org/10.1175/JAS3799.1.

Kuroda, Y., and K. Kodera, 2004: Role of the polar-night jet oscillation on the formation of the Arctic Oscillation in the Northern Hemisphere winter. *J. Geophys. Res.*, **109**, D11112, https://doi.org/10.1029/2003JD004123.

Labitzke, K., 1972: Temperature changes in the mesosphere and stratosphere connected with circulation changes in winter. *J. Atmos. Sci.*, **29**, 756–766, https://doi.org/10.1175/1520-0469(1972)029<0756:TCITMA>2.0.CO;2.

Lee, J. N., D. L. Wu, G. L. Manney, and M. J. Schwartz, 2009: Aura Microwave Limb Sounder observations of the northern annular mode: From the mesosphere to the upper troposphere. *Geophys. Res. Lett.*, **36**, L20807, https://doi.org/10.1029/2009GL040678.

Limpasuvan, V., J. H. Richter, Y. J. Orsolini, F. Stordal, and O.-K. Kvissel, 2012: The roles of planetary and gravity waves during a major stratospheric sudden warming as characterized by the WACCM. *J. Atmos. Sol.-Terr. Phys.*, **78-79**, 84–98, https://doi.org/10.1016/j.jastp.2011.03.004.

Liu, H.-L., and R. G. Roble, 2002: A study of a self-generated stratospheric sudden warming and its mesospheric–lower

thermospheric impacts using the coupled TIME-GCM/CCM3. *J. Geophys. Res.*, **107**, 4695, doi:10.1029/2001JD001533.

——, and ——, 2005: Dynamical coupling of the stratosphere and mesosphere in the 2002 Southern Hemisphere major stratospheric sudden warming. *Geophys. Res. Lett.*, **32**, L13804, https://doi.org/10.1029/2005GL022939.

Livesey, N. J., and Coauthors, 2015: Earth Observing System (EOS) Aura Microwave Limb Sounder (MLS) Version 4.2x Level 2 data quality and description document. Tech. Rep. JPL D-33509 Rev. B, Jet Propulsion Laboratory, California Institute of Technology, 169 pp., https://mls.jpl.nasa.gov/data/v4-2_data_quality_document.pdf.

Lott, F., and M. J. Miller, 1997: A new subgrid-scale orographic drag parameterization: Its foundation and testing. *Quart. J. Roy. Meteor. Soc.*, **123**, 101–127, https://doi.org/10.1002/qj.49712353704.

Manney, G. L., and Coauthors, 2008: The evolution of the stratopause during the 2006 major warming: Satellite data and assimilated meteorological analyses. *J. Geophys. Res.*, **113**, D11115, https://doi.org/10.1029/2007JD009097.

——, and Coauthors, 2009: Aura Microwave Limb Sounder observations of dynamics and transport during the record-breaking 2009 Arctic stratospheric major warming. *Geophys. Res. Lett.*, **36**, L12815, https://doi.org/10.1029/2009GL038586.

Matsuno, T., 1971: A dynamical model of the stratospheric sudden warming. *J. Atmos. Sci.*, **28**, 1479–1494, https://doi.org/10.1175/1520-0469(1971)028<1479:ADMOTS>2.0.CO;2.

Matthewman, N., J. Esler, A. J. Charlton-Perez, and L. M. Polvani, 2009: A new look at sudden stratospheric warmings. Part III: Polar vortex evolution and vertical structure. *J. Climate*, **22**, 1566–1585, https://doi.org/10.1175/2008JCLI2365.1.

McLandress, C., and T. G. Shepherd, 2009: Impact of climate change on stratospheric sudden warmings as simulated by the Canadian Middle Atmosphere Model. *J. Climate*, **22**, 5449–5463, https://doi.org/10.1175/2009JCLI3069.1.

——, J. F. Scinocca, T. G. Shepherd, M. C. Reader, and G. L. Manney, 2013: Dynamical control of the mesosphere by orographic and nonorographic gravity wave drag during the extended northern winters in 2006 and 2009. *J. Atmos. Sci.*, **70**, 2152–2169, https://doi.org/10.1175/JAS-D-12-0297.1.

Miller, A., H. Schmidt, and F. Bunzel, 2013: Vertical coupling of the middle atmosphere during stratospheric warming events. *J. Atmos. Sol.-Terr. Phys.*, **97**, 11–21, https://doi.org/10.1016/j.jastp.2013.02.008.

Mirzaei, M., C. Zülicke, A. R. Mohebalhojeh, F. Ahmadi-Givi, and R. Plougonven, 2014: Structure, energy, and parameterization of inertia–gravity waves in dry and moist simulations of a baroclinic wave life cycle. *J. Atmos. Sci.*, **71**, 2390–2414, https://doi.org/10.1175/JAS-D-13-075.1.

Mitchell, D. M., A. J. Charlton-Perez, and L. J. Gray, 2011: Characterizing the variability and extremes of the stratospheric polar vortices using 2D moment analysis. *J. Atmos. Sci.*, **68**, 1194–1213, https://doi.org/10.1175/2010JAS3555.1.

——, L. J. Gray, J. Anstey, M. P. Baldwin, and A. J. Charlton-Perez, 2013: The influence of stratospheric vortex displacements and splits on surface climate. *J. Climate*, **26**, 2668–2682, https://doi.org/10.1175/JCLI-D-12-00030.1.

Orsolini, Y. J., J. Urban, D. P. Murtagh, S. Lossow, and V. Limpasuvan, 2010: Descent from the polar mesosphere and anomalously high stratopause observed in 8 years of water vapor and temperature satellite observations by the Odin sub-millimeter radiometer. *J. Geophys. Res.*, **115**, D12305, https://doi.org/10.1029/2009JD013501.

Pedatella, N. M., H.-L. Liu, F. Sassi, J. Lei, J. L. Chau, and X. Zhang, 2014a: Ionospheric variability during the 2009 SSW: Influence of the lunar semidiurnal tide and mechanisms producing electron density variability. *J. Geophys. Res. Space Physics*, **119**, 3828–3843, https://doi.org/10.1002/2014JA019849.

——, and Coauthors, 2014b: The neutral dynamics during the 2009 sudden stratosphere warming simulated by different whole atmosphere models. *J. Geophys. Res. Space Physics*, **119**, 1306–1324, https://doi.org/10.1002/2013JA019421.

Pérot, K., J. Urban, and D. P. Murtagh, 2014: Unusually strong nitric oxide descent in the Arctic middle atmosphere in early 2013 as observed by Odin/SMR. *Atmos. Chem. Phys.*, **14**, 8009–8015, https://doi.org/10.5194/acp-14-8009-2014.

Quiroz, R. S., 1969: The warming of the upper stratosphere in February 1966 and the associated structure of the mesosphere. *Mon. Wea. Rev.*, **97**, 541–552, https://doi.org/10.1175/1520-0493(1969)097<0541:TWOTUS>2.3.CO;2.

Reichler, T., J. Kim, E. Manzini, and J. Kröger, 2012: A stratospheric connection to the Atlantic climate variability. *Nat. Geosci.*, **5**, 783–787, https://doi.org/10.1038/ngeo1586.

Ren, S., S. M. Polavarapu, S. R. Beagley, Y. Nezlin, and Y. J. Rochon, 2011: The impact of gravity wave drag on mesospheric analyses of the 2006 stratospheric major warming. *J. Geophys. Res.*, **116**, D19116, https://doi.org/10.1029/2011JD015943.

Richter, J. H., F. Sassi, and R. R. Garcia, 2010: Toward a physically based gravity wave source parameterization in a general circulation model. *J. Atmos. Sci.*, **67**, 136–156, https://doi.org/10.1175/2009JAS3112.1.

Scherhag, R., 1952: Die explosionsartigen Stratosphärenerwärmungen des Spätwinters 1951/52. *Ber. Dtsch. Wetterdienstes US-Zone*, **6** (38), 51–63.

Schmidt, H., and Coauthors, 2006: The HAMMONIA chemistry climate model: Sensitivity of the mesopause region to the 11-year solar cycle and CO_2 doubling. *J. Climate*, **19**, 3903–3931, https://doi.org/10.1175/JCLI3829.1.

Schoeberl, M. R., 1978: Stratospheric warmings: Observations and theory. *Rev. Geophys. Space Phys.*, **16**, 521–538, https://doi.org/10.1029/RG016i004p00521.

Seviour, W. J., D. M. Mitchell, and L. J. Gray, 2013: A practical method to identify displaced and split stratospheric polar vortex events. *Geophys. Res. Lett.*, **40**, 5268–5273, https://doi.org/10.1002/grl.50927.

Shepherd, M., S. R. Beagley, and V. I. Fomichev, 2014: Stratospheric warming influence on the mesosphere/lower thermosphere as seen by the extended CMAM. *Ann. Geophys.*, **32**, 589–608, https://doi.org/10.5194/angeo-32-589-2014.

Sigmond, M., J. F. Scinocca, V. Kharin, and T. G. Shepherd, 2013: Enhanced seasonal forecast skill following stratospheric sudden warmings. *Nat. Geosci.*, **6**, 98–102, https://doi.org/10.1038/ngeo1698.

Siskind, D. E., S. D. Eckermann, J. P. McCormack, L. Coy, K. W. Hoppel, and N. L. Baker, 2010: Case studies of the mesospheric response to recent minor, major and extended stratospheric warmings. *J. Geophys. Res.*, **114**, D00N03, doi:10.1029/2010JD014114.

Tan, B., X. Chu, H.-L. Liu, C. Yamashita, and J. M. Russell, 2012: Zonal-mean global teleconnection from 15 to 110 km derived from SABER and WACCM. *J. Geophys. Res.*, **117**, D10106, https://doi.org/10.1029/2011JD016750.

Tomikawa, Y., 2010: Persistence of easterly wind during major stratospheric sudden warmings. *J. Climate*, **23**, 5258–5267, https://doi.org/10.1175/2010JCLI3507.1.

——, K. Sato, S. Watanabe, Y. Kawatani, K. Miyazaki, and M. Takahashi, 2012: Growth of planetary waves and the formation of an elevated stratopause after a major stratospheric sudden warming in a T213L256 GCM. *J. Geophys. Res.*, **117**, D16101, https://doi.org/10.1029/2011JD017243.

Vignon, E., and D. M. Mitchell, 2015: The stratopause evolution during different types of sudden stratospheric warming event. *Climate Dyn.*, **44**, 3323–3337, https://doi.org/10.1007/s00382-014-2292-4.

von Storch, H., and F. W. Zwiers, 2003: *Statistical Analysis in Climate Research*. Cambridge University Press, 484 pp.

Watanabe, S., Y. Kawatani, Y. Tomikawa, K. Miyazaki, M. Takahashi, and K. Sato, 2008: General aspects of a T213L256 middle atmosphere general circulation model. *J. Geophys. Res.*, **113**, D12110, doi:10.1029/2008JD010026.

Xu, X., A. H. Manson, C. E. Meek, T. Chshylkova, J. Drummond, C. Hall, D. Riggin, and R. Hibbins, 2009: Vertical and interhemispheric links in the stratosphere–mesosphere as revealed by the day-to-day variability of Aura-MLS temperature data. *Ann. Geophys.*, **27**, 3387–3409, https://doi.org/10.5194/angeo-27-3387-2009.

Zülicke, C., and D. H. W. Peters, 2008: Parameterization of strong stratospheric inertia–gravity waves forced by poleward-breaking Rossby waves. *Mon. Wea. Rev.*, **136**, 98–119, https://doi.org/10.1175/2007MWR2060.1.

——, and ——, 2010: On the estimation of persistence in geophysical time series. *Eur. Phys. J. Spec. Top.*, **187**, 101–108, https://doi.org/10.1140/epjst/e2010-01275-2.

——, and E. Becker, 2013: The structure of the mesosphere during sudden stratospheric warmings in a global circulation model. *J. Geophys. Res. Atmos.*, **118**, 2255–2271, doi:10.1002/jgrd.50219.